Revision 1

Title

Effect of alkalinity on sulfur concentration at sulfide saturation in hydrous basaltic andesite to shoshonite melts at 1270 °C and 1 GPa.

Authors

Rameses J. D'Souza, Dante Canil*

School of Earth and Ocean Sciences, University of Victoria, Victoria, British Columbia, V8W 3P6, Canada

*dcanil@uvic.ca

1. Abstract

We have measured the effect of alkalis on S concentration at sulfide saturation (SCSS) in an underexplored compositional space of natural hydrous arc melts (basaltic andesite to shoshonite) at 1270°C and 1 GPa. At an oxygen fugacity approximately 2.5 log units below the fayalite-magnetite-quartz (FMQ) buffer, SCSS increases with Na_2O (562 ppm S/wt.% Na_2O), K_2O (98 ppm S/wt.% K_2O) and total alkalis (88 ppm S/wt.% Na_2O+K_2O) over the compositional range we have studied (1.6 – 3.1 wt.% Na_2O; 0 – 6.5 wt.% K_2O; 1.9 – 6.3 wt.% FeO^{tot}). Experiments with ~1.3 wt.% H_2O show approximately two-fold less increase in SCSS with alkalinity compared to those with ~ 3.0 wt.% H_2O. Our results show a possible limit to the increase in SCSS solely by increasing alkali concentration at ~7.5 wt.% total alkali concentration. Using our results and published data, we retrained earlier SCSS models to provide a better fit to test data. We also developed a new empirical model using theoretical optical basicity as a compositional parameter that predicts SCSS in the overall dataset with slightly better accuracy compared to previous models:

This is a preprint, the final version is subject to change, of the American Mineralogist (MSA)
Cite as Authors (Year) Title. American Mineralogist, in press.
DOI: https://doi.org/10.2138/am-2018-6404

$$ln(SCSS_{ppm}) = 16.34 - \frac{5784}{T} - 339.4\frac{P}{T} + 10.85ln(\Lambda) + 3.750X_{FeO} + 6.703X_{H_2O}$$

with temperature (T) in Kelvin, pressure (P) in GPa, the optical basicity (Λ) and mole fractions (X) of FeO (calculated from Kress and Carmichael, 1991) and H_2O in the melt. The discrepancies between observed and predicted SCSS for our experiments of varying alkalinity reflects the heavy bias toward anhydrous, alkali-poor basalt compositions in the underlying data sets on which most models are developed.

2. Introduction

Sulfur plays an important role in the geosphere by the formation of sulfide minerals or immiscible sulfide melts (e.g. Naldrett, 1969) which partition chalcophile elements (e.g. Cu, Pb, Zn) between silicate melts and sulfide phases, thereby controlling the movement of these elements between the mantle and crust, or in ore deposit generation (e.g. Sillitoe, 2010). The release of S into the atmosphere by degassing magmas is also important due to its impact on global climate (e.g. Scaillet and Macdonald, 2006; McLinden *et al.*, 2016). Sulfur is also used in industrial processes as sulfate in glass fining and as sulfide in glass colouring (e.g. Falcone *et al.*, 2011).

The geochemical behaviour of S in melts has a long history of study starting with Fincham and Richardson (1954) who used simple systems at 100 kPa to show that at log f_{O2} < ~5.5, S^{2-} displaces O^{2-} anions in silicate and aluminate melts by the reaction:

$$S^{2-}_{(silicate\ melt)} + \tfrac{1}{2}O_{2\ (gas)} = O^{2-}_{(silicate\ melt)} + \tfrac{1}{2}S_{2\ (gas)} \qquad [1]$$

Haughton *et al.* (1974) discovered that S Concentration at Sulfide Saturation (SCSS) is strongly correlated with Fe concentration and temperature in natural melts, described by Mavrogenes and O'Neill (1999) with the reaction:

$$FeS_{(sulfide)} + 0.5O_2 = 0.5S_2 + 2FeO_{(melt)} \qquad [2]$$

Several other experimental studies also show that SCSS increases with increasing temperature and decreasing pressure and is also sensitive to f_{O2} and melt composition (e.g. Shima and Naldrett, 1975; Danckwerth *et al.*, 1979; Wendlandt, 1982; Bradbury, 1983; Buchanan *et al.* 1983; Carroll and Rutherford, 1985, 1987, 1988; Mavrogenes and O'Neill, 1999; Holzheid and Grove, 2002; O'Neill and Mavrogenes, 2002; Clemente *et al.*, 2004; Jugo *et al.*, 2005a; Scaillet and Pichavant, 2005; Tsujimura and Kitakaze, 2005; Scaillet and Macdonald, 2006; Liu *et al.*, 2007; Jugo, 2009; Jugo et al., 2010; Ariskin *et al.*, 2013; Fortin *et al.*, 2015). In particular, SCSS is negatively correlated with SiO_2 (e.g. Holzheid and Grove, 2002) and shows a U-shaped dependance on melt FeO content with a minimum between ~1 and 8 wt.% FeO (O'Neill and Mavrogenes, 2002; Tsujimura and Kitakaze, 2005; Wykes *et al.*, 2015) where SCSS has little dependance on melt FeO. SCSS is also positively correlated with H_2O in the melt (Fortin *et al.*, 2015).

Dissolution of S in silicate melts can occur by the substitution of S^{2-} for non-bridging oxygen (NBO) in the melt via reaction [1]. It therefore follows that increasing the proportion of network-modifying cations (Fe^{2+}, Ca^{2+}, Mg^{2+}, Na^{+} and K^{+}), thus increasing NBO/T - the amount of NBO relative to tetrahedral oxygen (T) - at constant temperature, pressure and melt FeO, should also increase the SCSS of a melt. The alkali elements Na and K form network modifying cations of particular interest as they are known to affect several physical and chemical properties of melts, such as viscosity (Isard, 1969; Day, 1976) and NBO/T (Isard, 1969; Mysen *et al.*, 1985). The latter effect can increase the concentration of S^{2-} in a melt through reaction [1], although SCSS in melts is generally small enough that NBO are unlikely to be a limiting factor in S dissolution. Melt alkalinity is also known to increase the Fe^{3+}/Fe^{2+} of a melt at a given f_{O2} (e.g. Paul and Douglas, 1965; Gwinn and Hess, 1989; Cicconi *et al.*, 2015), which can increase the S^{6+}/S^{2-} of a melt (Jenner *et al.*, 2010) due to the stoichiometry of the equilibrium between $Fe^{2+} - Fe^{3+}$ and $S^{2-} - S^{6+}$ redox couples in the melt:

$$SO_4^{2-} + 8Fe^{2+}O = S^{2-} + 8Fe^{3+}O_{1.5} \quad [3]$$

Because S^{6+} can be up to 10 times higher concentration in a melt than S^{2-} (e.g. Carroll and Rutherford, 1985, 1987; Jugo *et al.*, 2005b), the higher Fe^{3+}/Fe^{2+} of an alkaline melt may increase SCSS by increasing S^{6+}/S^{2-}. The results of Klimm *et al.* (2012) show that the S^{6+}/S^{2-} transition at 0.2 GPa is indeed shifted to lower f_{O2} by ~1.5 log units in alkaline melts compared to basalts.

Alkali-rich magma series are found in all tectonic settings (e.g. Gupta, 2015) and, in arcs, are found with increasing distance from the trench (i.e. increasing height above the subducting plate (Dickinson, 1985). Alkali-rich rocks like shoshonites are an overall minor constituent of volcanic arcs, but can be associated with porphyry Cu deposits of economic interest (e.g. Müller and Groves, 1993; Mcinnes and Cameron, 1994; Lang *et al.*, 1995; Sillitoe, 2010; Logan and Mihalynuk, 2014), suggesting a possible link between alkalinity and the transport of S and chalcophile elements in arc magmatic systems. A compilation of volcanic rocks (n > 42,000; Sarbas and Nohl, 2008) from arcs worldwide reveals extensive variation total alkali concentration as low as 1.5 wt.% and up to 10 wt.% in basaltic andesites to tephriphonolites from the low-K to shoshonite series (Figure 1). There are positive correlations of S and alkalinity in arc melt inclusions (Ducea *et al.*, 1994), with up to 0.3 wt.% S in the oxidized alkalic melt inclusions of the Roman Province (Metrich and Clocchiatti, 1996), though these results may be due to changes in fO2. Scaillet and Macdonald (2006) showed a strong positive correlation of SCSS with alkalinity in hydrous rhyolite melts, however, no work has yet tested whether the effect of alkalinity in less evolved magmas.

The objective of the present study is to systematically study the effect of alkali concentration on SCSS in arc-like hydrous basaltic andesite to shoshonite compositions, ultimately to assess the potential role of alkali-rich magmas in transporting S in the arc setting. Because SiO_2 is the chief network former in natural magmas and is known to strongly impact SCSS, we restricted our study to compositions with ~51 wt.% SiO_2 where there is a relative paucity of experimentation on SCSS at high alkali concentration (Figure 1). Similarly, we restrict our study to starting materials with intermediate

FeO^{tot} (6 – 8 wt.%), near the broad minimum in the U-shaped dependence of SCSS on FeO^{tot} (O'Neill and Mavrogenes, 2002) to avoid changes in SCSS due to melt FeO^{tot}.

3. Methods

3.1 Starting materials

To examine the effect of alkalinity on SCSS in hydrous arc-like melts, we synthesized five starting materials with ~51 wt.% SiO_2; 6 – 8 wt.% FeO^{tot} and with varying total alkali concentration (Figure 1, Table 1). The concentration of Na_2O and K_2O in the starting materials varies from 1.5 – 3.1 wt.% and 0 – 6.2 wt.%, respectively, to capture the range of alkali concentrations in natural arc basaltic andesites to shoshonites (Figure 1). Other major element concentrations in our starting materials are similarly within the range of natural arc volcanic rocks containing ~51 wt.% SiO_2 (Table 1). To synthesize each starting material, reagent grade oxides (SiO_2, TiO_2, Al_2O_3, Fe_2O_3 and MgO) and carbonates ($CaCO_3$, Na_2CO_3 and K_2CO_3) were weighed out, mixed by shaking for 15 minutes, loaded into platinum crucibles, decarbonated and then fused at 1400°C for 12 hours, quenched to a glass, extracted and ground to a powder with an agate pestle and mortar. The glass powder was then fused for a further 12 hours, optically examined to ensure complete vitrification and homogeneity and then re-ground to a powder. Gibbsite, $Al(OH)_3$, and $FeSO_4$ were added to the glass powder, with further grinding for 5 minutes under ethanol in an agate mortar and pestle, to add 3.5 and 1 wt.% H_2O and S, respectively. The addition of $Al(OH)_3$ and $FeSO_4$ also introduces Al and Fe to the starting materials, and the final concentrations of all the oxides are listed in Table 1. The powders were then stored at 80°C before use. For three experiments (noted in Table 2), we reduced the H_2O content in the starting material by heating for 2 hours at 400°C to convert gibbsite ($Al(OH)_3$ – 35 wt.% H_2O) to boehmite (AlOOH – 15 wt.% H_2O; Zhu *et al.*, 2010) prior to loading into capsules.

3.2 Experimental procedure

120 Because S is highly reactive, the choice of capsule material is critical. The conditions of the
121 experiments (1 GPa, 1270ºC) precluded the use of Au (Akella and Kennedy, 1971). Platinum is
122 unsatisfactory due to severe Fe loss from the silicate melt to the capsule material, thus changing the
123 melt composition and affecting SCSS. We found that $Au_{75}Pd_{25}$ capsules failed in experiments longer
124 than four hours due to the formation of PdS alloy, which melts at 600ºC thereby rupturing the capsule,
125 and shorter duration experiments did not saturate in sulfide or sulfate. We therefore used 5 mm long
126 graphite capsules, with a cylindrical cavity 2 mm in diameter and 3 mm in length, loaded with
127 approximately 6 mg of starting material and sealed with snugly fitting graphite lids. The graphite
128 capsules were placed into 3 mm (outer diameter) Pt capsules and sealed by welding. The overall length
129 of the sealed Pt capsule was 6 mm. At 1270°C, the size of the thermal gradient is not significant issue
130 in our experiments as measurements in our apparatus have shown that the thermal gradient at 1400°C is
131 less than 20°C/mm, and this decreases with temperature, in agreement with other studies (e.g. Watson
132 *et al.*, 2002).
133 The sealed Pt capsules were held in the centre of a 30 mm long graphite furnace on MgO spacers.
134 The junction of a WRe_5-WRe_{26} ('Type C') thermocouple was positioned 3 mm from the centre of the
135 graphite furnace, separated from the Pt capsule by a 0.5 mm thick MgO disc, with the thermocouple
136 wires otherwise protected by four-bore tubing made of high purity alumina. The capsule and graphite
137 heater were placed within a 12.7 mm (outer diameter) $BaCO_3$ pressure assembly, wrapped in thin Pb
138 foil to reduce friction with the pressure vessel. Experiments were performed at 1270ºC and 1 GPa in an
139 end-loaded piston cylinder apparatus with temperature controlled by a programmable Eurotherm PID
140 controller which maintained experiment temperature to within 2ºC. Pressure was manually controlled
141 to within 0.02 GPa over the duration of each experiment. Friction correction for the $BaCO_3$ cells was
142 determined to be less than 2% based on the melting point of Au at 1 GPa (Akella and Kennedy, 1971).
143 A small 150 μm thick Pt wire was placed with the starting materials in two experiments (P479 and
144 P480) to estimate the f_{O2} using the solubility of Fe in Pt (Médard *et al.*, 2008).

145 For each experiment, the sample was pressurized to 0.5 GPa at ambient temperature and left for one
146 hour. Temperature was then raised to 600°C at 40°C/min and held for 6 minutes at 0.5 GPa, after which
147 the temperature was raised to 1270°C at 120°C/min. Pressure was gradually increased during the
148 second temperature ramp, reaching 1 GPa less than one minute after reaching experimental run
149 temperature. Experiments were quenched by shutting off power to the furnace, causing cooling at an
150 initial rate of ~2500°C/minute and coming to room temperature in approximately 90 seconds. Capsules
151 were extracted from the pressure assembly, mounted in 2.5 cm epoxy mounts and polished to expose
152 the capsule and its contents in longitudinal section.
153
154 *3.3 Electron Probe Micro-Analysis*
155 Chemical compositions of the experimental run products (Table 3) were determined by Electron
156 Probe Micro-Analysis (EPMA) at the University of British Columbia (UBC; Cameca SX-50) and the
157 University of Alberta (UA; Cameca SX-100). At UBC, major elements in glass were analyzed using a
158 beam diameter of 10 μm, beam current of 20 nA, accelerating voltage of 15 kV, with peak and
159 background count times of 20 and 10 seconds, respectively. The S concentration in glass was
160 determined with the same conditions but using 100 nA beam current with peak and background
161 counting times of 240 and 120 seconds, respectively. The following standards were used: albite, Na
162 (measured first); spinel, Al; diopside, Mg, Ca and Si; orthoclase, K; rutile, Ti; synthetic fayalite, Fe;
163 pyrite, S. On the UA instrument, major elements and S in glass were analyzed using a beam diameter of
164 10 μm, beam current of 70 nA, accelerating voltage of 15 kV, with peak and background count times of
165 30 seconds (120 seconds for S). The UA instrument used the following standards: albite, Na;
166 labradorite, Al; diopside, Mg, Ca and Si; sanidine, K; rutile, Ti; marcasite, Fe and S. For each
167 instrument, 10 – 15 points were selected on each glass, away from sulfide droplets. Sulfide droplets
168 were not analyzed as they were often too small (< 5 μm). To ensure internal consistency, three glasses
169 were analyzed with both the UBC and UA instruments. These duplicate analyses (listed in Table 3) are

within error of each other for major elements and S, except for P478, where there is a ~7% discrepancy between the UA and UBC analyses which we consider to be minor. Multiple analyses of the VG-2 Juan de Fuca MORB glass standard (Smithsonian microbeam standard NMNH 111240-52) over several sessions gives an average of 1521 ± 82 ppm, within the range of recommended values for this material (1397 ± 172 ppm; Table 3), demonstrating the accuracy of the S analyses. Platinum wires were analyzed in experiments P479 and P480 (Table A-1) at UBC using a beam diameter of 5 μm, a beam current of 100 nA, accelerating voltage of 15 kV with peak count times of 60 seconds for Fe and 30 seconds for Pt, with background count time of half the peak count time for these elements. The following standards were used for the metal analyses: pyrite, Fe; elemental metal, Pt.

3.4 Estimating alkali loss during EPMA

Exposure to a high current, small diameter electron beam during EPMA of hydrous silica-rich glasses can lead to significant under-reporting of the alkali elements, particularly Na, due to their migration away from the beam (Morgan and London, 1996, 2005). This phenomenon results in artificially low alkali concentration and correspondingly low analytical totals and it is important to assess the extent to which our analyses are affected by alkali migration during beam exposure. Time dependent intensity (TDI) corrections for Na, K, Si, Al and S were carried out for analyses done at UA using the Probe for EPMA Xtreme Edition software (Table A-2). TDI corrected concentrations of these elements are within error of the uncorrected values for all experiments except for Na_2O in P476. The difference between the TDI corrected and uncorrected Na_2O concentration of P476 is ~7% and is considered minor (Morgan and London 2005). Although TDI correction was not carried out at the UBC lab, the good agreement in analytical results from glasses analyzed at UA and UBC indicates that alkali loss is also not significant in the UBC analyses. In the discussion that follows, we use only the uncorrected alkali concentrations from the UA and UBC instruments.

195 *3.5 H_2O measurement by Raman spectroscopy*

196 Water content in experimental glasses may be estimated in a few different ways. Although H_2O
197 content cannot be directly measured by EPMA, the difference of the sum of analyzed elements from
198 100 may be taken an indirect measure of the H_2O content of a glass. This 'by difference' method,
199 however, is prone to errors associated with alkali loss during beam exposure, particularly for glasses
200 with > 70 wt.% SiO_2 (Morgan and London, 1996, 2005). As discussed above, applying TDI corrections
201 to our analyses shows little to no difference from uncorrected results indicating that the analyses are not
202 affected by alkali loss. Nevertheless, the 'by difference' method is still not ideal as it is only an indirect
203 measure of H_2O.

204 Micro-FTIR spectroscopy is a direct means of measuring H_2O in glass but cannot be used in our
205 experiments due to the presence of sulfide droplets throughout the glass. A recently developed means of
206 directly measuring H_2O in glasses relates the area of the OH stretching band at ~3550 cm^{-1} (A_w) in the
207 Raman spectra to the glass H_2O content (Behrens *et al.*, 2006). Le Losq *et al.* (2012) show that
208 normalizing A_w to the area of the Raman peaks relating to the glass silicate structure, from 100 – 1200
209 cm^{-1} (A_s), obviates compositionally dependent modification of the OH stretching band, thereby
210 negating the need for compositionally matched calibration standards (e.g. Behrens *et al.*, 2006). The
211 relationship between A_w/A_s and glass H_2O concentration demonstrated by Le Losq *et al.* (2012) is
212 highly linear (to within 0.2 wt.%, 2σ). This method of H_2O measurement, calibrated for instrument
213 differences (e.g. spectrometer CCD, grating etc.), was used by Fortin *et al.* (2015) in determining the
214 H_2O concentration of glasses in their SCSS experiments.

215 We obtained Raman spectra of our glasses using a Renishaw inVia confocal Raman microscope at
216 the University of Victoria using a 532 nm laser, 1200 line/mm grating and its 50x objective lens. At the
217 start of each analytical session the spectrometer was calibrated on the ~520 cm^{-1} peak of a Si wafer.
218 The position of the atmospheric N_2 Raman peak (~2330 cm^{-1}) served as another indicator of
219 spectrometer calibration over the course of each analytical session. Spectra were obtained from 100 to

4000 cm^{-1} with an acquisition time of 60 seconds. The laser was focused on the sample surface and set to 10% power to avoid damaging the glasses. Three acquisitions were accumulated for each glass to maximize the signal-to-noise ratio in the resulting spectrum. The raw Raman spectra were corrected for temperature and frequency-dependent scattering as per Long (1977) and to improve baseline correction prior to peak fitting (Behrens *et al.*, 2006; Le Losq *et al.*, 2012). A linear baseline from ~3000 cm^{-1} to ~3800 cm^{-1} was subtracted from the spectra and four Gaussian peaks were fit to the OH band at ~3550 cm^{-1} for each glass. In 100 – 1200 cm^{-1} region, the baseline subtracted was defined as a cubic spline anchored on the spectrum at ~200 cm^{-1}, ~640 cm^{-1}, ~800 cm^{-1} and ~1220 cm^{-1} as per Le Losq *et al.* (2012), and Gaussian peaks were fit to the resulting baseline-corrected spectra (Figure A-1). Baseline subtraction, peak fitting and area calculation were done using fityk (version 1.3.1). Because we did not have a range of glasses with independently known H_2O content with which to calibrate the slope of the A_w/A_s vs. H_2O relationship for the instrument we used, we initially applied the Le Losq *et al.* (2012) calibration. Measured in this way, the H_2O content of a MORB glass with known H_2O content (ALV1833-1, 2.14 ± 0.26 wt.% H_2O determined by FTIR; Stolper and Newman, 1994) is 3.6 ± 0.2 wt.% H_2O. This overestimate of 59% relative to the known H_2O content of ALV1833-1 is unsurprising as the Le Losq *et al.* (2012) calibration is specific to the Raman instrument those authors used. we therefore corrected H_2O concentrations obtained from the Le Losq *et al.* (2012) calibration by a factor of 0.59 and tested the accuracy of this correction by measuring an andesite glass with H_2O content known (Run 84, 3.80 ± 0.32 wt.% H_2O measured by FTIR; Mandeville *et al.*, 2002). The corrected analysis of the Run 84 glass is 4.59 ± 0.62 wt% H_2O, within error of the H_2O concentration determined by FTIR, indicating that this correction method is appropriate. Because the A_w/A_s relationship with H_2O content is independent of bulk composition (Le Losq *et al.*, 2012), the use of a MORB glass to determine the correction factor for the Le Losq *et al.* (2012) calibration for the instrument we used does not pose a problem for the varying alkali content of basaltic andesite glasses that we measure in this study.

The H_2O concentrations for the glasses in this study are listed in Table 3. As an indicator of precision, the glass in experiment P470 was measured in multiple sessions, giving an average A_w/A_s of 5.7 ± 0.6, and H_2O concentration of 2.43 ± 0.32 wt.%. The H_2O concentrations determined by Raman spectroscopy are within 0.5 wt.% of the 'by difference' method (Figure 2). The H_2O in the glasses of experiments P479 and P480 could nto be determined by Raman due to excessive fluorescence. Although not ideal, we use the 'by difference' method as an estimate of H_2O content of the glass in the two latter experiments.

4. Results

Experimental run products consisted of glass and < 5 μm spherical sulfide droplets (Figure A-2). No bubbles are observed. Some experiments with RD0K starting material show a few pyroxene crystals (visually estimated to be < 1 % by mode) in addition to glass and sulfide droplets (Table 2).

Experiments on the RD6K starting material of 1 and 4 hours duration (P466 and P474, respectively) have similar S contents within error (Table 3), implying that 1 hour is sufficient time for complete equilibration of S within the melt. The majority of sulfide-saturated experiments in the present study were of four hours duration (Table 2) which produced glasses with larger sulfide-free portions and thus easier to analyze by electron probe without beam overlap with disseminated sulfide droplets. Sulfur concentration in each glasses varies by < 15%,relative (2σ ; Table 3) indicating homogenous S concentration throughout the melt over the duration of the experiments.

The f_{O2} of two experiments in graphite capsules (P479, P480) was estimated using the solubility of Fe in Pt wire loops loaded in the charges. We measured the Fe content of the Pt wire along three lines from the centre of the wire to ~3 – 5 μm from the edge, using up to six spots per line (Table A-1). In each profile, the concentration of Fe in the Pt wire varies from near zero at the centre to ~9 – 10 wt.% near the edge, indicating that the wire is not completely homogenized in these experiments. We extrapolated the Fe content of the wire to the edge with melt to estimate the f_{O2} using the oxybarometer

of Médard *et al.* (2008). For P480, the projected Fe concentration at the Pt wire-melt interface (11.84 wt.% Fe) corresponds to log f_{O2} = -9.5 (i.e. ΔFMQ = -2.7; ΔCCO = -0.8). For P479, the projected Fe concentration at the Pt wire-melt interface (11.7 wt% Fe) corresponds to log f_{O2} = -9.2 (i.e. ΔFMQ = -2.4, ΔCCO = -0.5). Although these two experiments contained H_2O (3.3 – 3.5 wt.%), the f_{O2} estimates are within error of the lowest possible for anhydrous experiments in graphite-lined Pt capsules (i.e. ΔCCO = -0.8 ± 0.3; Medard *et al.*, 2008). We therefore infer that any oxidizing effect of H_2O on the f_{O2} of our experiments (e.g. Botcharnikov *et al.*, 2005), including those that were partially dehydrated, is negligible. In the calculations that follow, we take the average of the f_{O2} determinations for P480 and P479 (log f_{O2} = -9.35, ΔFMQ = -2.55, ΔCCO = -0.65) as the f_{O2} of all our experiments (Table 2).

The major element composition of the glasses (Table 3) is within 10% of the nominal composition of the starting materials as given in Table 1, except for FeO^{tot}. Two glasses (P479 and P480, marked in Figures 3, 4) have ~2 wt.% FeO^{tot}, reflect Fe loss from the melt into the Pt wire placed in these charges to monitor f_{O2}. In the remaining experiments, the glasses show FeO^{tot} concentrations of 4 – 6 wt.% (Figure 3a), which is ~1.8 wt.% less FeO^{tot} compared to the nominal composition of the starting materials (Table 1) and is attributable to partition of Fe into coexisting sulphide. Other than differences in FeO^{tot}, the similarity between the nominal starting material compositions and the measured glasses indicates that there was little loss of alkali elements by volatilization during fusion.

The major element concentration of the glasses varies chiefly in the concentration of FeO^{tot}, Al_2O_3, Na_2O and K_2O (Table 3). There is a weak, negative correlation between FeO^{tot} and SCSS in our experiments (R^2 = 0.06 and 0.27 for unmodified and partially dehydrated experiments, respectively; Figure 3a). The weakness of this correlation is expected given the broad, relatively flat inflection of the U-shaped FeO^{tot} vs. SCSS relationship between 1 and 8 wt.% FeO^{tot} (O'Neill and Mavrogenes, 2001; Wykes *et al.*, 2015).

Our results show SCSS negatively correlated with Al_2O_3, decreasing from 1540 ppm at 15.6 wt.% Al_2O_3 to 700 ppm at 19.5 wt.% Al_2O_3 (R^2 = 0.68; Figure 3b) for undehydrated experiments. The three

295 experiments that were partially dehydrated show little separation in Al_2O_3 content and no correlation is
296 observed with SCSS.

297 Alkali concentrations, individually and in total, are positively correlated with SCSS (Figure 3c-e).
298 The strongest correlation is between Na_2O and SCSS for unmodified and partially dehydrated
299 experiments, respectively (Figure 3c). The slope of the Na_2O-SCSS relationship is 562 ppm S/wt.%
300 Na_2O and 260 ppm S/wt.% Na_2O for both fully hydrous and partially dehydrated experiments. The
301 effect of K_2O on SCSS is over five times less than that of Na_2O or total alkali concentration in
302 experiments using unmodified starting materials (98 ppm S/wt.% K_2O, 88 S/wt.% Na_2O+K_2O (Fig.
303 3d). We use alkalinity, defined here as the molar ratio (Na+K)/Al to account for the co-variation of
304 Na_2O, K_2O and Al_2O_3 and find that it is positively related to SCSS (Figure 3f). Similar to the individual
305 and total alkali concentrations, the slope of the alkalinity-SCSS relationship for the experiments using
306 unmodified starting materials is approximately twice that of the partially dehydrated starting materials
307 (Fig. 3ef).

308 The concentration of H_2O in glasses from experiments for which starting materials were fully
309 hydrated are similar within error (2.4 – 3.1 wt.%; Table 3), except for P468 which shows 1.2 wt.%
310 H_2O, likely due to water loss during welding of the Pt capsule. Experiments for which the starting
311 materials were partially dehydrated all have H_2O concentrations of ~1.3 wt.%. Experiments with 2.4 –
312 3.1 wt.% H_2O (P474, P466, P476, P470) show higher SCSS than their partially dehydrated counterparts
313 with ~1.3 wt.% H_2O (P472, P478, P471) despite otherwise similar major element composition (Table
314 3). This effect in melts with lower H_2O results in an approximate decrease in the slope of the SCSS vs.
315 alkalis and alkalinity relationship by a factor of two (Figure 3c - f). Our results also show that SCSS
316 increases by ~250 ppm S/wt.% H_2O between the partially dehydrated and unmodified experiments of
317 moderate and high alkalinity (RD6K and RD4K; Figure 4). The lowest alkalinity experiments (RD0K)
318 on the other hand show a slope that is ten times lower (23 ppm S/wt.% H_2O) although the correlation is
319 poor. ($R^2 = 0.14$).

320

321 **5. Discussion**

322 *5.1 Effect of alkalinity on SCSS*

323 Our results indicate that SCSS increases with alkalinity and that the effect of Na_2O is approximately
324 five times greater than that of K_2O in hydrous compositions (Figure 3c, d). No previous work has
325 directly examined changes in SCSS with increasing alkalinity. Previously published SCSS results at
326 similar SiO_2 concentration to our experiments (~52 – 56 wt.% SiO_2) vary up to ~9 wt.% total alkalis
327 and ~4 wt.% K_2O (Figure 1). The only published SCSS results with comparable SiO_2 and FeO^{tot} as our
328 data are from Peach *et al.* (1994). The range of Na_2O 2.2 to 2.7 wt.% in their experiments is relatively
329 small, but correlates with SCSS ($R^2 = 0.81$). The increase in SCSS with Na_2O in the Peach et al. (1994)
330 experiments is twice that of our experiments (1059 vs. 562 ppm S/wt.% Na_2O, respectively), though
331 this may be attributed to the considerably higher temperature of those experiments (1450°C) compared
332 to this study. We found no experiments in the literature of published SCSS results to allow us to
333 compare our results on the effect of variable K_2O on SCSS.

334 The increase in SCSS that we observe in our experiments may be attributed to increased Fe^{3+}/Fe^{2+}
335 according to reaction [3] given that ferric iron is increasingly stabilized by high alkali element
336 concentrations at a given f_{O2} in silicate melts (Paul and Douglas, 1965; Gwinn and Hess, 1989, Cicconi
337 *et al.*, 2015). We have calculated Fe_2O_3/FeO using the Kress and Carmichael (1991) model, in which
338 the coefficients for the alkali elements require Fe_2O_3/FeO increases with alkalinity when all other
339 factors are constant. Contrary to Cicconi et al. (2015) we find that Na/(Na+K) is inversely correlated
340 Fe_2O_3/FeO (Table 3), which is unsurprising as our experiments examine low K to shosonite melt
341 compositions in which K_2O varies far greater than Na_2O (Table 1).

342 Reaction [3] above indicates that increasing Fe^{3+}/Fe^{2+} will strongly increase the S^{6+}/S^{2-} of a melt. As
343 S^{6+} is more soluble in melts (e.g. Jugo *et al.*, 2005b), small changes in S^{6+}/S^{2-} due to changes in
344 Fe^{3+}/Fe^{2+} caused by increasing alkalinity will increase concentration of SCSS. This interpretation

345 requires the presence of S^{6+} even at the reduced f_{O2} of our experiments, implying that increasing
346 alkalinity shifts the $S^{2-} - S^{6+}$ transition to lower f_{O2} than in basalts. However, fO2 estimates for our
347 experiments (FMQ-2.7) are ~1 log units lower than the onset of the $S^{2-} - S^{6+}$ transition in Fe-free,
348 alkaline glasses or in basalt (~FMQ-1 to FMQ- Klimm et al., 2012; Jugo et al , 2010) indicating that S
349 is likely predominantly present as S^{2-} and any increase in SCSS due to stabilization of S^{6+} may only be
350 minimal.

351 Given the strong dependence of SCSS on FeO^{tot} (O'Neill and Mavrogenes, 2002; Wykes et al., 2015),
352 it may be argued that the increase in SCSS that we observe is due to small changes in FeO^{tot} of our
353 melts (1.9 – 6.3 wt.%) and not due to alkalinity. Our data, however, do not show any relationship
354 between FeO^{tot} and SCSS (Figure 3a). Furthermore, the range of FeO^{tot} in our experiments is within the
355 relatively flat and wide inflection of the U-shaped SCSS relationship with FeO^{tot} between ~1 and 8
356 wt.% FeO^{tot}, as observed by Mavrogenes and O'Neill (2002) and Wykes *et. al* (2015). Thus, the
357 variation in FeO^{tot} in our experiments is not expected to greatly impact SCSS.

358 Our data shows an apparent peak in SCSS with increasing alkalinity (Figure 3e) with the highest
359 alkalinity experiments showing lower SCSS than moderate alkalinity ones. We observe this apparent
360 peak in SCSS in experiments using both fully hydrated and partially dehydrated starting materials.
361 Experiment P476 (7.3 wt.% total alkalis) shows 200 – 300 ppm more S than the highest alkalinity
362 experiments P466 and P474 (8.5 – 9.3 wt.% total alkalis) and experiment P478 (7.4 wt.% total alkalis)
363 shows 180 ppm more S than P472 (9.0 wt.% total alkalis). This observation implies that there may be a
364 limit to the increase in SCSS solely as a function of alkalinity.

365

366 *5.2 Previous SCSS models and alkalinity*

367 Modelling of SCSS as a function of temperature, pressure and melt composition has been a goal of
368 many studies. Mavrogenes and O'Neill (1999) used regression analysis to derive an empirical SCSS
369 model equation rooted in the thermodynamics of S^{2-} dissolution in silicate melts. Although those

370 authors recognized the importance of melt composition on SCSS, their work in a restricted
371 compositional space consideration only P and T. O'Neill and Mavrogenes (2002) conducted a large
372 number of experiments at 1400°C and 1 bar to determine the effect of composition on SCSS in the
373 CMAS ± Fe ± Ti system and found that SCSS was strongly inversely correlated with FeO^{tot} at < ~1
374 FeO^{tot} but increased with increasing FeO^{tot} above ~8 wt.% FeO^{tot} (i.e. an asymmetric U-shaped
375 relationship). Holzheid and Grove (2002) noted that the degree of melt polymerization strongly
376 controlled the SCSS and used the NBO/T ratio, to account for this in their model, based on data from
377 anhydrous experiments. Scaillet and Pichavant (2005) presented a model for melt S content, that
378 included a term for H_2O and six terms to account for T, P, f_{S2}, f_{O2} and a single compositional term
379 embodying 10 oxide species terms. Liu *et al.* (2007) used a model of the form presented by
380 Mavrogenes and O'Neill (1999), but used 'MFM' to parameterize the melt composition. The MFM
381 parameter correlates positively with NBO/T and is modified from the M and FM parameters initially
382 used to predict zircon and rutile saturation, respectively (Watson and Harrison, 1983; Ryerson and
383 Watson, 1987). The MFM value for a melt is calculated as:

384 $$MFM = \frac{Na+K+2(Ca+Mg+Fe^{2+})}{Si(Al+Fe^{3+})} \quad [4]$$

385 using the mole fractions of each element and calculating Fe^{2+} and Fe^{3+} by the method of Kress and
386 Carmichael (1991). The negative dependence of SCSS on melt FeO content (at low FeO) was included
387 in the empirical model Li and Ripley (2005) developed for anhydrous compositions, although those
388 authors removed this term in an updated model (Li and Ripley, 2009) that also accounted for H_2O.
389 The effect of H_2O on SCSS was explicitly tested and parameterized by Fortin *et al.* (2015) who
390 present two empirical SCSS models that account for H_2O: one, an update of the Liu *et al.* (2007) MFM
391 model, and a second model based on linear regression of oxide species present in the melt. Finally, we
392 note that Ni or Cu in sulphide melt has an impact on SCSS (Ariskin *et al.* (2013); Smythe et al, 2017).
393 The relatively low concentration of Ni compared to Fe in natural melts implies that, though the

394 formation of Fe-Ni-Cu complexes will shift SCSS, the effect will be relatively minor compared to other
395 variables such as FeO^{tot} (Smythe et al, 2017). Indeed, Fortin *et al.* (2015) found that their oxide species
396 model predicted SCSS in Ni-bearing melts to within 5%, thus avoiding the need to separately
397 parameterize the Fe-Ni-S solution mechanism. In what follows, we refer to the models of Liu *et al.*
398 (2007), Li and Ripley (2009) and Fortin *et al.* (2015) as these are recent SCSS models that are based
399 on, and their predictions compare well against, larger and more comprehensive datasets than older
400 models.

401 In general, no single MFM-based model is consistently better than any other in predicting the SCSS
402 of our experiments (Figure 5a). The Liu *et al.* (2007) model consistently deviates from the measured
403 SCSS by > 30% from measured SCSS. The Fortin *et al.* (2015) MFM model best predicts the SCSS in
404 melts with high alkali concentration (alkalinity > 0.6), deviating by < 15% from the measured SCSS.
405 The Fortin *et al.* (2015) MFM model deviates by -30 – +70% at alkalinity < 0.4. Comparing the oxide
406 species models that we consider (Figure 5b), the Fortin *et al.* (2015) model is generally more successful
407 at predicting the SCSS of our experiments, deviating by 25 – 45% at low alkalinity to ~-40% at high
408 alkalinity. The Li and Ripley (2009) model performs best for low alkalinity glasses, underestimating
409 SCSS by < 25%, however this model underestimates the observed SCSS by up to 70% in higher
410 alkalinity experiments. Both sets of models, MFM-based and oxide-based, show discrepancies between
411 predictions and observations that have an approximately parabolic, concave-up geometry with
412 increasing alkalinity, with minima at (Na+K)/Al = 0.4 – 0.5 for the MFM model.

413 Part of the reason these models inconsistently predict the effects of alkalinity on SCSS is due to the
414 heavy bias toward anhydrous MORB-like compositions in the data sets on which those models are
415 calibrated (Figure 1). As discussed above, the effect of alkalinity on SCSS has not been systematically
416 studied, resulting in sparse coverage of the high alkali compositional space relative to other
417 compositions (Figure 1), particularly for 52 – 56 wt.% SiO_2 melts of this study, resulting in very large
418 bias in the models. Although our experiments are on the outer limits of the compositional space of

419 previous SCSS experiments, they are within the realm of high-K or shoshonite series magmas in arcs
420 (Figure 1b). Therefore, to increase the calibrated range of SCSS models, we have used our new
421 experimental results to retrain the two models presented by Fortin *et al.* (2015), as these are the most
422 recent, and present a model of our own in the following sections.
423
424 *5.3 Updates to previous models*
425 As discussed above and by Fortin *et al.* (2015), H_2O has a significant control on SCSS. We therefore
426 use the dataset compiled by Fortin *et al.* (2015), containing only data from the literature where the H_2O
427 content of sulfide-bearing melts was directly measured, together with the results that we present in this
428 study. The dataset comprises the 13 results from this study, 10 from sulfide-bearing experiments carried
429 out in graphite-lined Pt capsules from Wykes *et al.* (2015), 18 of Fortin *et al.* (2015) and the 234 results
430 compiled by those authors (Baker *et al.*, 2001; Beermann *et al.*, 2011; Brenan, 2008; Ding *et al.*, 2014;
431 Haughton *et al.*, 1974; Holzheid and Grove, 2002; Jugo *et al.*, 2005a, Liu *et al.*, 2007; Mavrogenes and
432 O'Neill, 1999; Moune *et al.*, 2009; Peach and Mathez, 1993; Peach *et al.*, 1994; Righter *et al.*, 2009;
433 Sattari *et al.*, 2002). Although there are a great many SCSS measurements, we have not included all of
434 them in our database primarily because they did not measure glass H_2O content directly or because they
435 used very different bulk compositions (see Fortin *et al.* 2015 for details). The sulfide-bearing
436 experiments done in Re capsules by Wykes *et al.* (2015) were not included in our data compilation as
437 those authors were unable to constrain the lower f_{O2} limit of those experiments. The dataset was
438 randomly split into a training subset (n= 209) including all the SCSS data from the present study, and a
439 verification subset (n=66), a 3:1 split of the overall dataset.
440 We determined coefficients to the parameters of the MFM and oxide species models (Table 4)
441 presented by Fortin *et al.* (2015), using linear regression and 10-fold cross-validation, repeated 10
442 times, with the R package 'caret' (R Core Team, 2017; Kuhn, 2017). The retrained MFM model is:

This is a preprint, the final version is subject to change, of the American Mineralogist (MSA)
Cite as Authors (Year) Title. American Mineralogist, in press.
DOI: https://doi.org/10.2138/am-2018-6404

443
$$ln(SCSS_{ppm}) = 10.55 - \frac{5081}{T} - 366.7\frac{P}{T} + 0.4653lnMFM + 0.3276lnX_{FeO} + 2.967X_{H_2O} \quad [5]$$

444 with T in Kelvin, P in GPa, and X_i being the mole fraction of oxide i. The coefficients to equation [5]
445 are within error of those presented by Fortin *et al.* (2015), but the updated MFM model provides a
446 slightly reduced fit to the training dataset, with an $R^2 = 0.791$ and $\chi^2 = 3.29$ for the updated model
447 compared to 0.807 and 3.71, respectively, for the old model. The updated MFM model, however,
448 performs well on the randomly selected verification dataset ($R^2 = 0.855$, $\chi^2 = 0.879$). The average
449 squared residual in the training dataset for the updated MFM model is similar to that of the original
450 model (0.11).

451 The updated oxide species model is:

452
$$ln(SCSS_{ppm}) = 36.05 - \frac{6115}{T} - 363.3\frac{P}{T} - 21.01X_{H_2O} - 26.68X_{SiO_2} - 19.97X_{TiO_2} - 27.34X_{Al_2O_3} - 18.10X_{FeO^{tot}} - 23.71X_{MgO} - 21.08X_{CaO} - 23.51X_{Na_2O} - 26.69X_{K_2O} \quad [6]$$

453 with T, P and X_i as above. The coefficients to equation [6] are also within error of those presented by
454 Fortin *et al.* (2015), and the updated and original oxide species models reproduce their training datasets
455 similarly well: $R^2 = 0.904$ and $\chi^2 = 1.49$ for the updated model compared to 0.918 and 1.56,
456 respectively, for the original model. The updated model also performs well in predicting SCSS of the
457 verification dataset ($R^2 = 0.929$, $\chi^2 = 0.432$). The average squared residual for the training dataset for
458 the updated oxide model (0.05) is similar to the original model (0.04). The greatest difference between
459 the oxide species model coefficients presented by Fortin *et al.* (2015) and our updated version are for
460 Na_2O and K_2O, though they are still within error.

461 The updated MFM model shows negligible improvement in predicting SCSS of our experiments
462 (Figure 5a), with SCSS predictions that are consistently 10 – 15% lower than the Fortin *et al.* (2015).
463 The updated MFM model shows smaller differences between predicted and observed SCSS at low
464 alkalinity, but slightly greater difference at high alkalinity. The updated oxide species model is more

obviously improved compared to the original, giving SCSS predictions that are ~25% lower than observed SCSS at high alkalinity (Figure 5b). The updated oxide species model fares as well as the original Fortin *et al.* (2015) oxide model at low alkalinity, overestimating SCSS by upto ~50%.

5.4 Developing a new model

We chose to develop a new SCSS model based on the MFM model of Liu *et al.* (2007), updated by Fortin *et al.* (2015). Models relying on universal melt descriptors depend on the linearity of the relationship between observed SCSS and the chosen compositional parameter. The MFM parameter (equation [4]) was chosen by Liu *et al.* (2007) on this basis and correlates positively with NBO/T. In natural log space, MFM shows a linear relationship against observed SCSS for the experiments in the Fortin *et al.* (2015) compilation (Figure 6a). However, although the experiments from the present study show a strong linear trend with MFM, the separation in their MFM values accounts for only 6% of the overall range of MFM in the database of previously publish SCSS results, even though our experiments vary from basaltic andesite to shoshonitic compositions. This relative lack of variation for such a large compositional shift may be why the MFM model performance with changing alkalinity is not greatly increased between the updated MFM model we present above and that presented by Fortin *et al.* (2015).

In an effort to find a compositional parameter that better reflects the variation in alkalinity of our experiments, we have assessed optical basicity (Λ, lamda), a universal melt descriptor used in material sciences to quantify the polymerization of slags. Optical basicity is essentially the weighted average of the negative charge borne by the cations in a melt (Mills, 1993). As per Mills (1993), Λ is calculated as:

$$\Lambda = \frac{\sum X_i n_i \Lambda_{th,i}}{\sum X_i n_i} \qquad [7]$$

where X_i is the mole fraction of oxide i, n is the number of O associated with i, $\Lambda_{th,\,i}$ is the theoretical Λ of i and the summation is over the different oxide species present in the melt. In the present work, we

used values for Λ_{th} for the oxide species (Table A-3) from Mills (1993) and Duffy (1996). The mole fractions of Fe_2O_3 and FeO were calculated using the Kress and Carmichael (1991) model which is calibrated on a dataset comprising an extremely wide range of SiO_2 and alkalinity, from ugandite to basalt and rhyolite, encompassing our experiment compositions. Botcharnikov *et al.* (2005) found that H_2O has a negligible effect on the Fe^{2+}/Fe^{3+} ratio of a melt, thus small variations in the H_2O content of our glasses will not significantly affect the mole fractions of Fe_2O_3 and FeO calculated using the Kress and Carmichael (1991) model. Similar to MFM, Λ also has a linear relationship with observed SCSS. However, because Λ accounts for the identity of the cation species via Λ_{th} in addition to their relative abundance, the high alkalinity glasses from our study have higher Λ compared to low alkalinity glasses (Table 3, Figure 6b). The range of Λ in our experiments accounts for ~13% of the variation in the overall database of previously published SCSS results.

We used Λ in an empirical SCSS model with the same form as the MFM model of Fortin *et al.* (2015):

$$lnSCSS_{ppm} = a + \frac{b}{T} + c\frac{P}{T} + dln\Lambda + eX_{FeO} + fX_{H_2O} \qquad [8]$$

where T is temperature in Kelvin, P is pressure in GPa, Λ is optical basicity calculated as above (equation [7]), X_{FeO} is the mole fraction of FeO calculated by the method of Kress and Carmichael (1991), and X_{H2O} is the mole fraction of H_2O. Fortin *et al.* (2015) used $\ln X_{FeOtot}$, however, we found that using X_{FeO} gave an improved fit (see Section 5.6 for the implications of this). We determined the coefficients to equation [8] (referred to hereafter as the OB model) by multiple linear regression with the R package 'caret' (R Core Team, 2017; Kuhn, 2017), using 10-fold cross-validation repeated 10 times, applied to the same training and verification datasets as used above to update the Fortin *et al.* (2015) models to include our new data. The resulting OB model is:

$$lnSCSS_{ppm} = 16.44 - \frac{6081}{T} - 379.8\frac{P}{T} + 10.61ln\Lambda + 3.533X_{FeO} + 6.601X_{H_2O} \qquad [9]$$

The digits presented for the coefficients and their standard errors in Table 5 are not intended to imply that level of precision but are presented to avoid rounding errors in implementation.

The OB model provides a good fit to the training dataset with R^2, χ^2 and mean squared residual values of 0.865, 2.13 and 0.07, respectively, and for the verification data set ($R^2 = 0.903$, $\chi^2 = 0.615$, mean squared residual = 0.06). The OB model predicts SCSS in the training and verification datasets to within 5 – 10% of the measured value in natural log space for all but one result at low SCSS (Figure 7a). This is equivalent to differences between predicted and observed SCSS of -50 – +125% over the full range of observed SCSS (Figure 7b), though in most cases the OB model overestimates SCSS by < 70% and underestimates it by < 35%.

The OB model reduces the spread of predicted SCSS for our experiments to within -10 – +60% of the observed SCSS, compared to -30 – +60% for the updated MFM model (Figure 8) and -25 – +60% for the Fortin *et al.* (2015) MFM model (Figure 7a). In detail, the Fortin *et al.* (2015) MFM model performs better at high alkalinity, predicting SCSS to within ±15%, compared to OB model predictions which deviate by -10 – +30% from the observed SCSS. In the lowest alkalinity glasses, the OB model fares better than either the Fortin *et al.* (2015) MFM model or our updated version of that model (equation [5]), with predictions ~ 5 – 20% closer to the actual SCSS than either of those models.

The difference between the observed and predicted SCSS is larger for the highest and lowest alkalinity experiments for the OB model but is within 10% of the observed SCSS at moderate alkalinity ((Na+K)/Al = 0.4 to 0.6; Figure 8). The same approximately parabolic geometry of discrepancy between predicted and observed SCSS with increasing alkalinity is seen in the MFM and oxide species models as well (Figure 6, 8), except vertically offset. A possible reason for the discrepancy may be gleaned from considering the range of compositions for which SCSS experiments have been carried out. Figure 1 shows that the silica and alkalinity range of published SCSS experiments is quite small when considering experiments for which H_2O concentrations have been directly measured. At low alkalinity, the majority of experiments are anhyrdous and basaltic compared to the hydrous, basaltic

andesite compositions studied here. Further, there is almost no previous work in the compositional vicinity of our highest alkalinity experiments. Thus, our experiments at the extremes of alkalinity are on the edge of the compositional space in which the models presented have been calibrated and it is to be expected that model performance will be degraded at these extremes (Figures 6, 8). On the other hand, our experiments at moderate to high alkalinity (i.e. (Na+K)/Al = 0.4 to 0.6) occupy a region of compositional space where the database of experiments shows the greatest co-variation of alkalis and SiO_2 (Figure 1). The OB model accordingly performs well at moderate alkalinity, predicting SCSS to within 10% of the observed value (Figure 8).

Lastly, it is also possible that the approximately parabolic shape of the misfit between observations and SCSS model predictions (Figures 5a, 8) is partly due to the form of the models used, thereby indicating a fundamental shortcoming in the models. However, we cannot conclusively determine whether sample bias in the datasets underlying the models or shortcomings of the model forms themselves plays a greater role in producing the observed misfit between obsereved and predicted SCSS with increasing alkalinity.

5.5 SCSS models and low FeO systems

Although the present work is focused on examining the effect of alkalinity on SCSS to update empirical models, we briefly comment on the models discussed here when applied to systems with low FeO^{tot} (i.e. < 1 wt.%). Mavrogenes and O'Neill (2002) show that melt FeO^{tot} is a dominant compositional control on SCSS at > ~8 and < ~1 wt.% FeO^{tot}. Wykes *et al.* (2015) showed that the MFM model and, by extension its variants (Liu *et al.* 2007); Fortin *et al.* 2015) are fundamentally unable to predict the increasing SCSS of low FeO^{tot} silicate melts as these models have a positive coefficient to the $\ln X_{FeO}$ term. We attempted to include the effect of low FeO^{tot} on SCSS in the OB model by including the SCSS experiments from O'Neill and Mavrogenes (2002) and Wykes *et al.* (2015) in the training datasets and by using a variety of terms to account for the ascending and

562 descending limbs of the SCSS vs FeO^{tot} relationship. The fit of our and other MFM models to the
563 training and verification datasets were severely reduced (typical R^2 values of ~0.5) likely due to the
564 very different compositions studied by O'Neill and Mavrogenes (2002) compared to the experiments
565 used here. Additionally, inclusion of the more than 200 experiments from O'Neill and Mavrogenes
566 (2002) skews the overall dataset to low pressure (100 kPa) and relatively high temperatures (1673 K),
567 thus biasing the models away from higher pressures and lower temperatures. Therefore, we have not
568 further considered the strong negative dependence of SCSS on FeO^{tot} in the present work, although we
569 recognize that the effect of low FeO on SCSS is undoubtedly important in granitic and rhyolitic
570 systems, for example.
571
572 **6. Conclusions and future work**
573 We have investigated the effect of alkali concentration on the SCSS of basaltic andesite to shoshonite
574 melts. Our results show an approximately two-fold increase in SCSS for melts with high alkalinity
575 (~1500 ppm S at (Na+K)/Al ≈ 0.6) compared to low alkalinity (~700 ppm S at (Na+K)/Al ≈ 0.15),
576 when other compositional parameters (i.e. SiO_2, FeO^{tot}, H_2O) are relatively unchanged. The effect of
577 Na_2O on SCSS is five times greater than that of K_2O in the investigated compositional range. An
578 apparent peak in SCSS with increasing alkalinity at a total alkali content of ~7.5 wt.% (i.e. (Na+K)/Al
579 ≈ 0.6), if due to changes in the melt environment that disfavour the dissolution of S as S^{6+}, is testable
580 by more experiments and detailed examination of the regions where S bonds are observed in Raman
581 spectra (200 – 1200 cm^{-1} and ~2600 cm^{-1}; e.g. Klimm *et al.*, 2012).
582 We used our new results to examine the performance of published empirical SCSS models. The
583 MFM model of Fortin *et al.* (2015) overestimate SCSS at low alkalinity by 40 – 70%, but performs
584 well with ~15% deviation from observed SCSS at high alkalinity. The Fortin *et al.* (2015) oxide species
585 model underestimates SCSS by ~40% at high alkalinity. Models trained on earlier datasets cannot fully
586 capture the variation in SCSS with alkalinity. Our new model, built on the work of Fortin *et al.* (2015),

587 employs theoretical optical basicity (OB) to account for the different identities of network modifiers
588 and network formers and not only their mole fractions. Compared with earlier models, the OB model
589 reduces the spread of SCSS predictions with changing alkalinity and also provides a slightly better fit
590 to the overall database of SCSS experiments for which H_2O concentration is directly measured.
591

592 **Acknowledgements**

593 We thank M. Raudsepp (UBC), E. Czech (UBC) and A. Locock (UA) for assistance with EPMA, A.
594 Brolo, A. Wlasenko and S. Konorov for assistance with the Raman measurements, and L. Coogan for
595 helpful discussions. We are also grateful to E. Cottrell for the use of her FTIR standard glasses in our
596 Raman work. We acknowledge the reviews from P. Jugo and an anonymous reviewer and of J. Wykes
597 on an earlier version of this manuscript. This work was supported by a National Sciences and
598 Engineering Research Council of Canada Discovery Grant to D. Canil.

599 **References**

600 Akella J. and Kennedy G. C. (1971) Melting of gold, silver, and copper- proposal for a new high-
601 pressure calibration scale. J. Geophys. Res. 76, 4969-4977.
602
603 Ariskin A. A., Danyushevsky L. V., Bychkov K. A., McNeill A. W., Barmina G. S. and Nikolaev G. S.
604 (2013) Modeling solubility of Fe-Ni sulfides in basaltic magmas: The effect of Nickel. Econ. Geol.
605 108, 1983-2003.
606
607 Baker D.R., Barnes S.J., Simon G. and Bernier F. (2001) Fluid transport of sulfur and metals between
608 sulfide melt and basaltic melt. Can. Mineral. 39, 537-546.
609
610 Beermann O., Botcharnikov R.E., Holtz F., Diedrich O. and Nowak M. (2011) Temperature
611 dependence of sulfide and sulfate solubility in olivine-saturated basaltic magmas. Geochim. et
612 Cosmochim. Act. 75, 7612-7631.
613
614 Behrens H., Roux J., Neuville D.R. and Siemann M. (2006) Quantification of dissolved H2O in silicate
615 glasses using confocal microRaman spectroscopy. Chem. Geol. 229, 96-112.
616
617 Botcharnikov, R. E., Koepke, J., Holtz, F., McCammon, C., Wilke, M. (2005) The effect of water
618 activity on the oxidation and structural state of Fe in a ferro-basaltic melt. Geochim. et Cosmochim.
619 Act. 69, 5071-5085.
620
621 Bradbury J. W. (1983) Pyrrhotite solubility in hydrous albite melts. Ph.D. thesis, Penn. State Univ.
622
623 Brenan J.M. (2008) Re–Os fractionation by sulfide melt–silicate melt partitioning: a new spin. Chem.
624 Geol. 248, 140-165.
625
626 Buchanan D.L., Nolan J., Wilkinson N. and de Villiers J.R. (1983) An experimental investigation of
627 sulphur solubility as a function of temperature in synthetic silicate melts. In Geol. Soc. South Africa
628 Spec. Pub. 7, 383-391.
629
630 Carroll M. R. and Rutherford M. J. (1985) Sulfide and sulfate saturation in hydrous silicate melts. J.
631 Geophys. Res. 90, C601-C612.
632
633 Carroll M. R. and Rutherford M. J. (1987) The stability of igneous anhydrite: experimental results and
634 implications for sulfur behaviour in the 1982 El Chicon trachyandesite and other evolved magmas. J.
635 Petrol. 28, 781-801.
636
637 Carroll M. R. and Rutherford M. J. (1988) Sulfur speciation in hydrous experimental glasses of varying
638 oxidation state: results from measured wavelength shifts of sulfur X-rays. Am. Mineral. 73, 845-849.
639
640 Cicconi M. R., Giuli G., Ertel-Ingrisch W., Paris E. and Dingwell D. B. (2015) The effect of the
641 [Na/(Na+K)] ratio on Fe speciation in phonolitic glasses. Am. Mineral. 100, 1610-1619.
642
643 Clemente B., Scaillet B. and Pichavant M. (2004) The solubility of sulphur in hydrous rhyolitic melts.
644 J. Petrol. 45, 2171-2196.
645
646 Danckwerth, P. A., Hess, P. C., and Rutherford, M. J. (1979) The Solubility of Sulfur in High-TiO2
647 Mare Basalt. In Proceedings of the 10th Lunar and Planetary Science Conference, 517–530.

Day D.E. (1976) Mixed alkali glasses-their properties and uses. J. Non Cryst. Solids 21, 343-372.

Dickinson, W.R. (1975) Potash-depth (K-h) relations in continental margin and intra-oceanic magmatic arcs. Geology, 3, 53-56.

Ding S., Dasgupta R. and Tsuno K. (2014) Sulfur concentration of martian basalts at sulfide saturation at high pressures and temperatures–implications for deep sulfur cycle on Mars. Geochim. Cosmochim, Act. 131, 227-246.

Ducea M. N., McInnes B. I. A. and Wyllie P. J. (1994) Sulfur variations in glasses from volcanic rocks: effect of melt composition on sulfur solubility. Int. Geol. Rev. 36, 703-714.

Duffy J.A. (1996) Optical basicity: A practical acid-base theory for oxides and oxyanions. J. Chem. Educ. 73, 1138-1142.

Falcone R., Ceola S., Daneo A. and Maurina S. (2011) The role of sulfur compounds in colouring and melting kinetics of industrial glass. In Sulfur in magmas and melts: its importance for natural and technical processes, 73 (eds. H. Behrens and J. D. Webster) Mineral. Society of America, pp. 113-139.

Fincham C. J. B. and Richardson, F. D. (1954) The behaviour of sulphur in silicate and aluminate melts. Proc. R. Soc. Lond. 223A, 40-62.

Fortin M.-A., Riddle J., Desjardins-Langlais Y. and Baker D. R. (2015) The effect of water on the sulfur concentration at sulfide saturation (SCSS) in natural melts. Geochim. Cosmochim. Acta 160, 100-116.

Gómez-Tuena, A., Mori, L., Goldstein, S.L. and Pérez-Arvizu, O. (2011) Magmatic diversity of western Mexico as a function of metamorphic transformations in the subducted oceanic plate. Geochim. Cosmochim. Act. 75, 213-241.

Gupta A. K. (2015) Origin of potassium-rich silica-deficient igneous rocks. Springer, India.

Gwinn R. and Hess P. C. (1989) Iron and titanium solution properties in peraluminous and peralkaline rhyolitic liquids. Contrib. Mineral. Petrol. 101, 326-338.

Haughton D. R., Roeder P. L. and Skinner B. J. (1974) Solubility of sulfur in mafic magmas. Econ. Geol. 69, 451-467.

Holzheid A. and Grove T. L. (2002) Sulfur saturation limits in silicate melts and their implications for core formation scenarios for terrestrial planets. Am. Mineral. 87, 227-237.

Isard J. O. (1969) The mixed alkali effect in glass. J. Non Cryst. Solids 1, 235-261.

Jenner F.E., O'Neill H.S.C., Arculus R.J. and Mavrogenes J.A. (2010) The magnetite crisis in the evolution of arc-related magmas and the initial concentration of Au, Ag and Cu. J. Petrol. 51, 2445-2464.

Jugo P. J. (2009) Sulfur content at sulfide saturation in oxidized magmas. Geol. 37, 415-418.

Jugo P.J., Luth R.W. and Richards J.P. (2005a) An experimental study of the sulfur content in basaltic melts saturated with immiscible sulfide or sulfate liquids at 1300° C and 1· 0 GPa. J. Petrol. 46, 783-798.

Jugo P.J., Luth R.W. and Richards J.P. (2005b) Experimental data on the speciation of sulfur as a function of oxygen fugacity in basaltic melts. Geochim. Cosmochim. Act. 69, 497-503.

Klimm K., Kohn S.C., O'Dell L.A., Botcharnikov R.E. and Smith M.E. (2012) The dissolution mechanism of sulphur in hydrous silicate melts. I: Assessment of analytical techniques in determining the sulphur speciation in iron-free to iron-poor glasses. Chem. Geol. 322, 237-249.

Kress V. C. and Carmichael I. S. E. (1991) The compressibility of silicate liquids containing Fe2O3 and the effect of composition, temperature, oxygen fugacity and pressure on their redox states. Contrib. Mineral. Petrol. 108, 82-92.

Lang J. R., Lueck B., Mortensen J. K., Russell J. K., Stanley C. R. and Thompson J. F. H. (1995) Triassic-Jurassic silica-undersaturated and silica-saturated alkalic intrusions in the Cordillera of British Columbia: implications for arc magmatism. Geol. 23, 451-454.

LeBas M. J., Lemaitre R. W., Streckeisen A. and Zanettin B. (1986). A chemical classification of volcanic rocks based on the total alkali silica diagram. J. Petrol. 27, 745-750.

Le Losq C., Neuville D.R., Moretti R. and Roux J. (2012) Determination of water content in silicate glasses using Raman spectrometry: Implications for the study of explosive volcanism. Am. Mineral. 97, 779-790.

Lenoir M., Grandjean A., Poissonnet S. and Neuville D.R. (2009) Quantitation of sulfate solubility in borosilicate glasses using Raman spectroscopy. J. Non Cryst. Solids 355, 1468-1473.

Li C. and Ripley E.M. (2005) Empirical equations to predict the sulfur content of mafic magmas at sulfide saturation and applications to magmatic sulfide deposits. Miner. Deposita 40, 218-230.

Li C. and Ripley E.M. (2009) Sulfur contents at sulfide-liquid or anhydrite saturation in silicate melts: empirical equations and example applications. Econ. Geol. 104, 405-412.

Liu Y., Samaha N.-T. and Baker D.R. (2007) Sulfur concentration at sulfide saturation (SCSS) in magmatic silicate melts. Geochim. Cosmochim. Acta 71, 1783-1799.

Logan J. M. and Mihalynuk M. G. (2014) Tectonic controls on early mesozoic paired alkaline porphyry deposit belts (Cu-Au +/- Ag-Pt-Pd-Mo) within the Canadian Cordillera. Econ. Geol. 109, 827-858.

Long D.A. (1977) Raman Spectroscopy, 276 p. MacGraw-Hill, New York

Mandeville C.W., Webster J.D., Rutherford M.J., Taylor B.E., Timbal A. and Faure K. (2002) Determination of molar absorptivities for infrared absorption bands of H2O in andesitic glasses. Am. Mineral. 87, 813-821.

745 Mavrogenes J. A. and O'Neill H. St. C. (1999) The relative effects of pressure, temperature and oxygen
746 fugacity on the solubility of sulfide in mafic magmas. Geochim. Cosmochim. Acta 63, 1173-1180.
747
748 McInnes B. I. A. and Cameron E. M (1994) Carbonated, alkaline hybridizing melts from a sub-arc
749 environment: mantle wedge samples from the Tabar-Lihir-Tanga-Feni arc, Papua New Guinea. Earth
750 Planet. Sci. Lett. 122, 125-141.
751
752 McLinden C. A., Fioletov V., Shephard M. W., Krotkov N., Li C., Martin R. V., Moran M. D. and
753 Joiner J. (2016) Space-based detection of missing sulfur dioxide sources of global air pollution. Nat.
754 Geosci. 9, 496-500.
755
756 Médard E., McCammon C.A., Barr J.A. and Grove T.L. (2008) Oxygen fugacity, temperature
757 reproducibility, and H2O contents of nominally anhydrous piston-cylinder experiments using graphite
758 capsules. Am. Mineral. 93, 1838-1844.
759
760 Metrich N. and Clocchiatti R. (1996) Sulfur abundance and its speciation in oxidized alkaline melts.
761 Geochim. Cosmochim. Act. 60, 4151-4160.
762
763 Morgan G.B. and London D. (1996) Optimizing the electron microprobe analysis of hydrous alkali
764 aluminosilicate glasses. Am. Mineral. 81, 1176-1185.
765
766 Morgan G.B. and London D. (2005) Effect of current density on the electron microprobe analysis of
767 alkali aluminosilicate glasses. Am. Mineral. 90, 1131-1138.
768
769 Moune S., Holtz F. and Botcharnikov R.E. (2009) Sulphur solubility in andesitic to basaltic melts:
770 implications for Hekla volcano. Contrib. Mineral. Petrol. 157, 691-707.
771
772 Müller D. and Groves D. I. (1993) Direct and indirect associations between potassic igneous rocks,
773 shoshonites and gold-copper deposits. Ore Geol. Rev. 8, 383-406.
774
775 Mysen B. O. and Popp R. K. (1980) Solubility of sulfur in CaMgSi2O6 and NaAlSi3O8 melts at high
776 pressure and temperature with controlled fO2 and fS2. Am. J. Sci. 280, 78-92.
777
778 Mysen B.O., Virgo D. and Seifert F.A. (1982) The structure of silicate melts: implications for chemical
779 and physical properties of natural magma. *Rev. Geophys.* **20**, 353-383.
780
781 Mysen B. O., Virgo D. and Seifert, F. A. (1985) Relationships between properties and structure of
782 aluminosilicate melts. Am. Mineral. 70, 88-105.
783
784 Naldrett A. J. (1969) A portion of the system Fe-S-O between 900 and 1080°C and its application to
785 sulfide ore magmas. J. Petrol. 10, 171-201.
786
787 O'Neill H. St. C. and Mavrogenes J. A. (2002) The sulfide capacity and the sulfur content at sulfide
788 saturation of silicate melts at 1400°C and 1 bar. J. Petrol. 43, 1049-1087.
789
790 Paul A. and Douglas R.W. (1965) Ferrous–ferric equilibrium in binary alkali silicate glasses. Phys.
791 Chem. Glasses 6, 207–211.
792

Peach C.L. and Mathez E.A. (1993) Sulfide melt-silicate melt distribution coefficients for nickel and iron and implications for the distribution of other chalcophile elements. Geochim. Cosmochim. Act. 57, 3013-3021.

Peach C.L., Mathez E.A., Keays R.R. and Reeves S.J. (1994) Experimentally determined sulfide melt-silicate melt partition coefficients for iridium and palladium. Chem. Geol. 117, p. 361-377.

Reagan, M.K., Hanan, B.B., Heizler, M.T., Hartman, B.S. and Hickey-Vargas, R. (2008) Petrogenesis of volcanic rocks from Saipan and Rota, Mariana Islands, and implications for the evolution of nascent island arcs. J. Petrol. 49, 441-464.

Righter K., Pando K. and Danielson L.R. (2009) Experimental evidence for sulfur-rich martian magmas: Implications for volcanism and surficial sulfur sources. Earth Planet. Sci. Lett. 288, p. 235-243.

Ryerson F.J. and Watson E.B. (1987) Rutile saturation in magmas: implications for TiNbTa depletion in island-arc basalts. Earth Planet. Sci. Lett. 86, 225-239.

Sarbas B. and Nohl U. (2008) The GEOROC database as part of a growing geoinformatics network. In: Geoinformatics 2008-Data to Knowledge, Proceedings: U.S. Geological Survey Scientific Investigations Report 2008-5172 (eds. S. R. Brady, A. K. Sinha and L. C. Gundersen) pp. 42-43.

Sattari P., Brenan J.M., Horn I. and McDonough W.F. (2002) Experimental constraints on the sulfide- and chromite-silicate melt partitioning behavior of rhenium and platinum-group elements. Econ. Geol. 97, 385-398.

Scaillet B. and Macdonald R. (2006) Experimental and thermodynamic constraints of the sulphur yield of peralkaline and metaluminous silicic flood eruptions. J. Petrol. 47, 1413-1437.

Scaillet B. and Pichavant M. (2005) A model of sulphur solubility for hydrous mafic melts: application to the determination of magmatic fluid. Ann. Geophys. 48, 671-698.

Shima H. and Naldrett A.J. (1975) Solubility of sulfur in an ultramafic melt and the releveance of the system Fe-S-O. Econ. Geol. 70, 960-967.

Sillitoe R. H. (2010) Porphyry copper systems. Econ. Geol. 105, 3-41.

Stolper E. and Newman S. (1994) The role of water in the petrogenesis of Mariana trough magmas. Earth Planet. Sci. Lett. 121, 293-325.

Smythe, D.J., Wood, B.J., Kiseeva, E.S. (2017) The S content of silicate melts at sulfide saturation: New experiemnts and a model incorporating the effects of sulfide composition. Am. Mineral., 102, 795-803.

Tsujimura T. and Kitakaze A. (2005) Experimental study of sulfur solubility in silicate melts coexisting with graphite as a function of silicate melt composition. Res. Geol. 55, 55-60.

Watson E.B. and Harrison T.M. (1983) Zircon saturation revisited: temperature and composition effects in a variety of crustal magma types. Earth Planet. Sci. Lett. 64, 295-304.

Watson, E.B., Wark, D.A., Price, J.D. and Van Orman, J.A. (2002) Mapping the thermal structure of solid-media pressure assemblies. Contrib. Mineral. Petrol., 142, 640-652.

Wendlandt R. F. (1982) Sulfide saturation of basalt and andesite melts at high pressures and temperatures. Am. Mineral. 67, 877-885.

Wykes J. L., O'Neill, H. St. C. and Mavrogenes, J. A. (2015) The effect of FeO on the sulfur content at sulfide saturation (SCSS) and the selenium content and selenide saturation of silicate melts. J. Petrol. 56, 1407-1424.

Zhu, B., Fang, B., Li, X. (2010) Dehydration reactions and kinetic parameters of gibbsite. Ceramic International, 36, 2493-2498.

855 **Figure captions**

856 Figure 1: a) Total Alkali-Silica diagram (LeMaitre, 2002) and b) Potassium classification diagram
857 (LeBas *et al.*, 1986) showing the starting materials from the present study and the distribution of SCSS
858 experiments from the literature that we used in this study (see text for details) in the context of arc
859 lavas from around the world. Arc data from GEOROC (http://georoc.mpch-mainz.gwdg.de/georoc/;
860 Sarbas and Nohl, 2008). Experimental data (see text for details) are from Haughton *et al.* (1974), Peach
861 and Mathez (1993), Peach *et al.* (1994), Mavrogenes and O'Neill (1999), Baker *et al.* (2001), Holzheid
862 and Grove (2002), Sattari *et al.* (2002), Jugo *et al.* (2005a), Liu *et al.* (2007), Brenan (2008), Moune *et*
863 *al.* (2009), Righter *et al.* (2009), Beermann *et al.* (2011), Ding *et al.* (2014), Fortin *et al.* (2015) and
864 Wykes *et al.* (2015).
865
866 Figure 2: Comparison of H_2O measured directly by Raman spectroscopy and indirectly by EPMA (by
867 difference method). Experiment P468 shows low H_2O content most likely due to H_2O loss during Pt
868 capsule welding. Error bars are 2σ.
869
870 Figure 3: Bivariate diagrams showing S concentration in sulfide saturated glasses plotted against the
871 concentration of a) Al_2O_3; b) Na_2O; c) K_2O; d) molar Na + K / Al. Experiments that contained Pt wire
872 are marked with a small black square (see text for details). The solid lines are regressed through the
873 experiments using fully hydrated starting materials (equations near the top of each panel) whereas the
874 dashed lines are through partially dehydrated starting materials (equations near the bottom of each
875 panel). Error bars are 2σ and where they are not seen, the error bars are smaller than the symbols.
876
877 Figure 4: Variation of SCSS as a function of H2O in experiments where the starting materials were run
878 unmodified and after partial dehydration. Linear regression of the data are as follows (S in ppm, H_2O in
879 wt.%): RD0K, $S = 643.7 + 22.83 \cdot H_2O$ ($R^2 = 0.14$); RD4K, $S = 517.9 + 250.1 \cdot H_2O$ ($R^2 = 0.99$); RD6K,

880 $S = 708.1 + 247.6 \cdot H_2O$ ($R^2 = 0.96$), Experiments P479 and P480 are not shown as there were no
881 experiments performed using those starting materials after partial dehydration.
882
883 Figure 5: Percent difference between predicted and measured SCSS in our experiments plotted against
884 molar (Na + K)/Al for a) MFM parameterized models (Liu *et al.,* 2007; Fortin *et al.*, 2015, Model A)
885 and b) oxide species models (Li and Ripley, 2009; Fortin *et al.*, 2015, Model B). Also shown are the
886 results of the updated models using data from the present study. The light grey and dark grey regions
887 are 25% and 10% error envelopes, respectively.
888
889 Figure 6: SCSS in experimental glasses from this and previous work (see text and caption of Figure 1
890 for references) plotted as a function of a) MFM and b) optical basicity calculated using the formula
891 presented by Mills (1993) with the optical basicity values given by Mills (1993) and Duffy (1996). The
892 arrow point in the direction of increasing alkalinity of the glasses from the present study.
893
894 Figure 7: a) Predicted SCSS plotted against measured SCSS using the OB model for the training and
895 verification datasets. The solid line shows a 1:1 relationship (0% error) and the dashed and dotted lines
896 are 5% and 10% error envelopes respectively. b) The percent difference between modelled and
897 measured SCSS in training and verification datasets plotted against measured SCSS.
898
899 Figure 8: Percent difference between predicted and measured SCSS in our experiments plotted against
900 molar (Na + K)/Al for the OB model from the present study. Also shown are the results of the updated
901 MFM and oxide species models presented in this study. The light grey and dark grey regions are 25%
902 and 10% error envelopes, respectively.
903

Figure A-1: Representative examples of the Raman spectra that we obtained to quantify H_2O using the method as described in the text. The spectra are corrected and baseline subtracted. Although some structure is visible in the low wavenumber regions corresponding to the silicate structure, we are unable to determine from this data the relative intensities of peaks known to be related to S bonds (i.e. sulfate at 990 cm^{-1}, sulfide at 372 and 2574 cm^{-1}; Klimm *et al.*, 2012). We note the increase in intensity of a peak at 1080 cm^{-1} with increasing alkalinity.

Figure A-2: Back-scattered electron images of glasses from expriments a) P470 (RD0K), and b) P474 (RD6K), showing the different sizes and generally circular shape of sulfide droplets typical of the run products from this study. The white scale bar in both images represents 100 μm.

This is a preprint, the final version is subject to change, of the American Mineralogist (MSA)
Cite as Authors (Year) Title. American Mineralogist, in press.
DOI: https://doi.org/10.2138/am-2018-6404

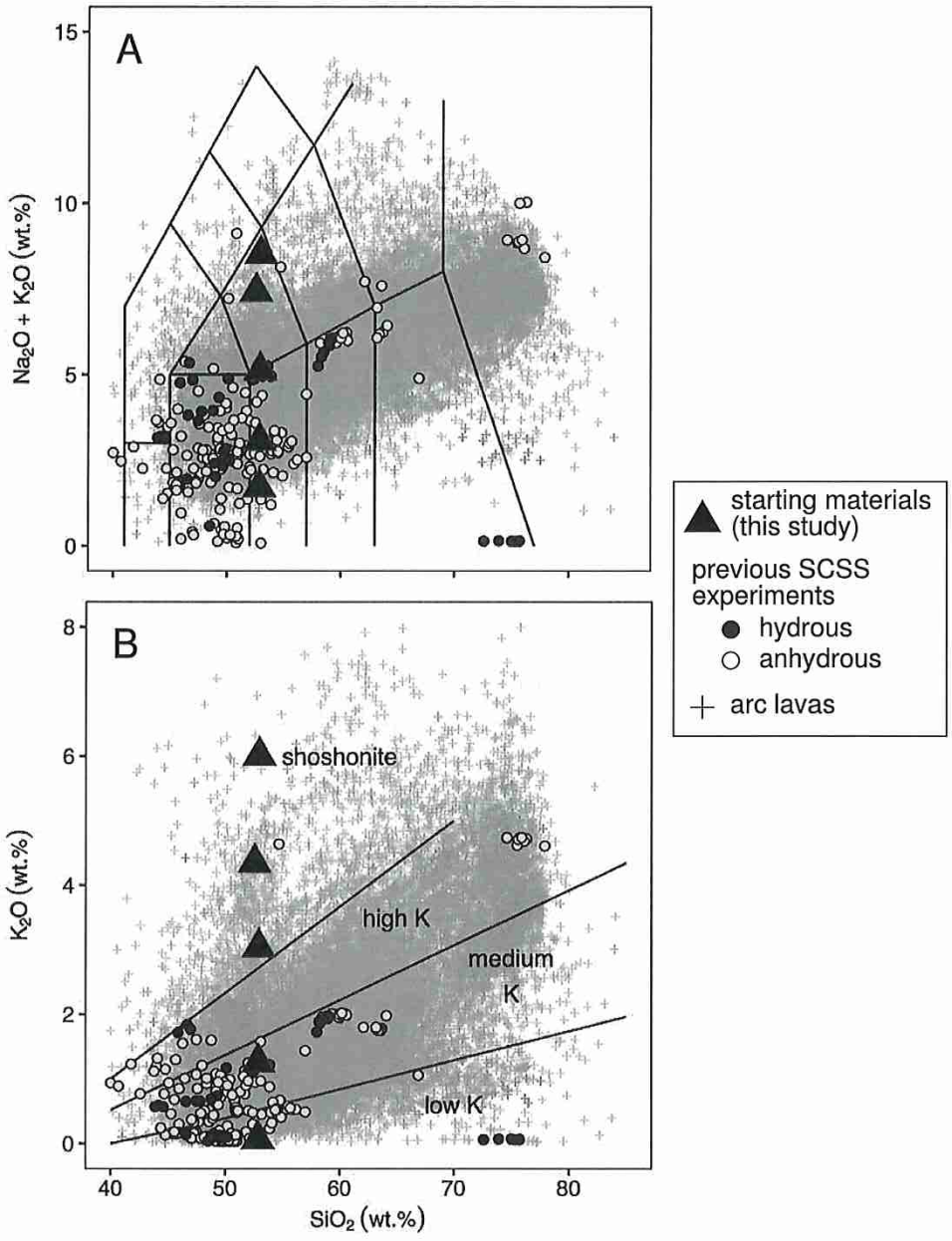

This is a preprint, the final version is subject to change, of the American Mineralogist (MSA)
Cite as Authors (Year) Title. American Mineralogist, in press.
DOI: https://doi.org/10.2138/am-2018-6404

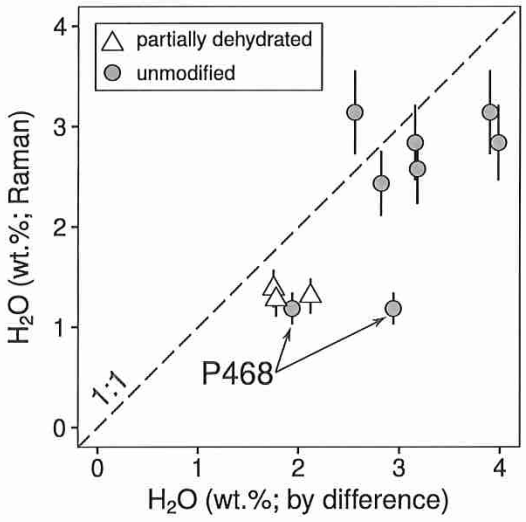

This is a preprint, the final version is subject to change, of the American Mineralogist (MSA)
Cite as Authors (Year) Title. American Mineralogist, in press.
DOI: https://doi.org/10.2138/am-2018-6404

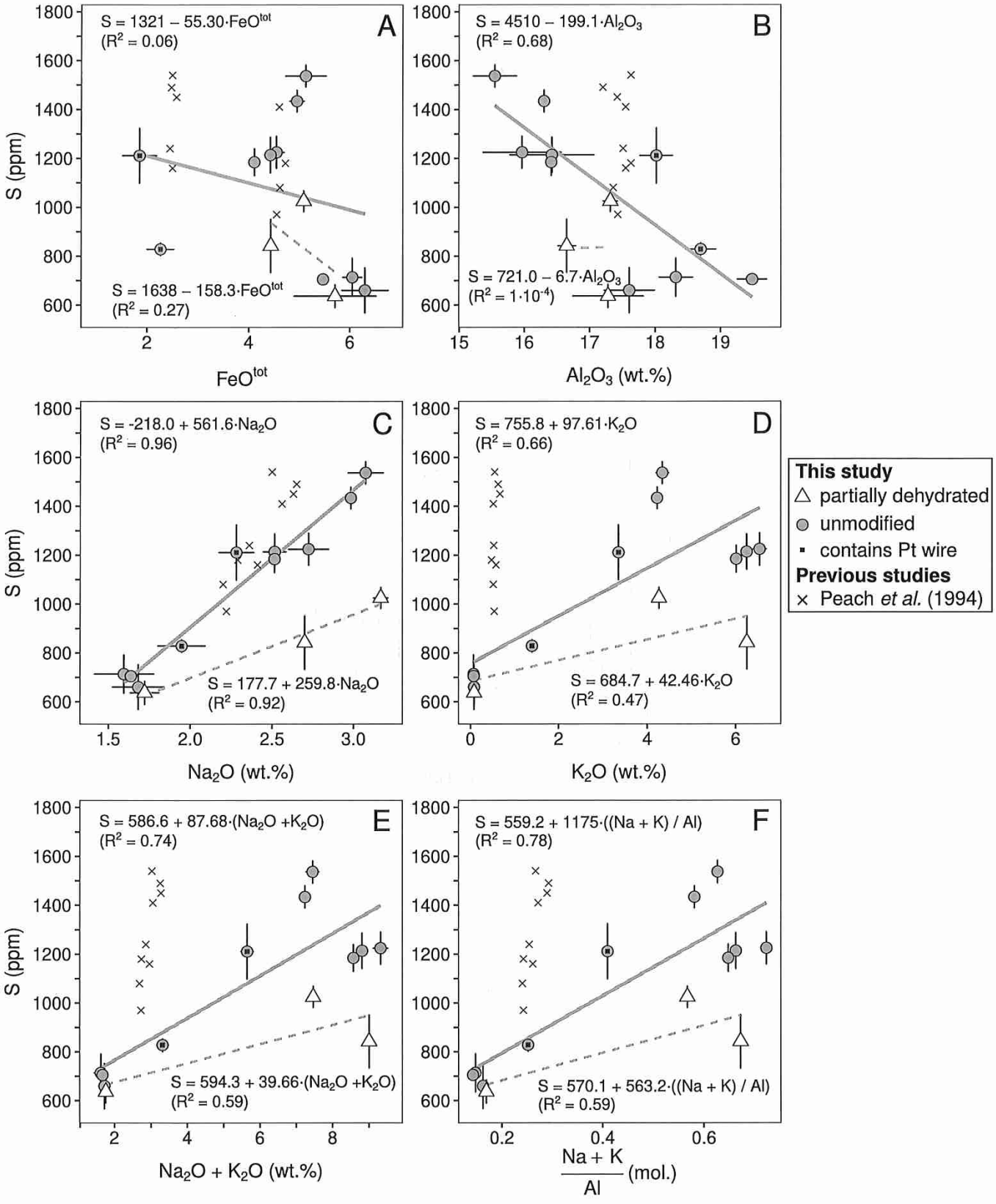

DOI: https://doi.org/10.2138/am-2018-6404

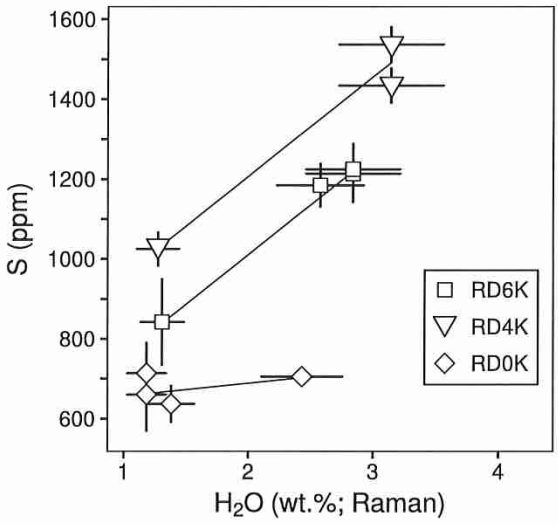

This is a preprint, the final version is subject to change, of the American Mineralogist (MSA)
Cite as Authors (Year) Title. American Mineralogist, in press.
DOI: https://doi.org/10.2138/am-2018-6404

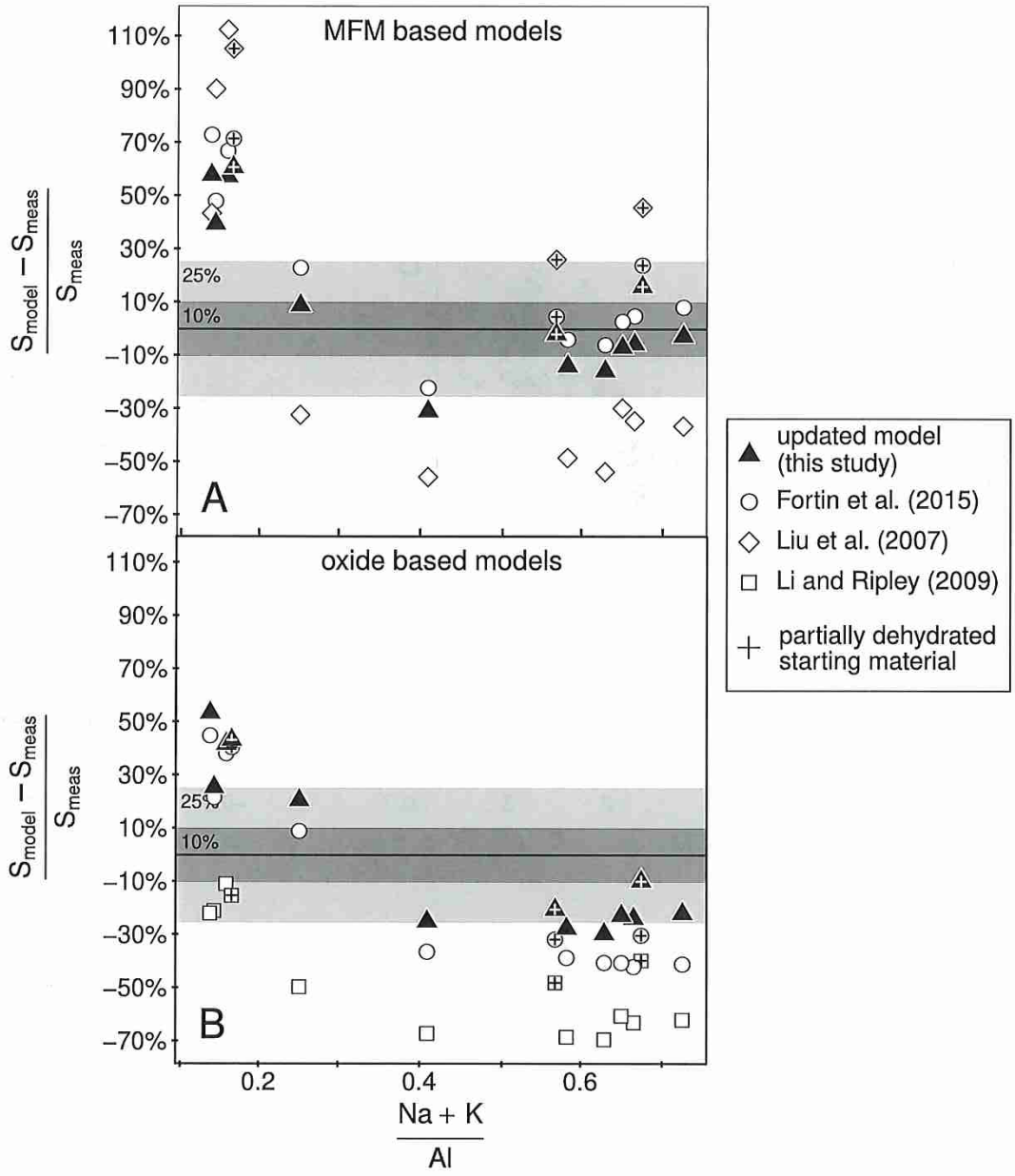

This is a preprint, the final version is subject to change, of the American Mineralogist (MSA)
Cite as Authors (Year) Title. American Mineralogist, in press.
DOI: https://doi.org/10.2138/am-2018-6404

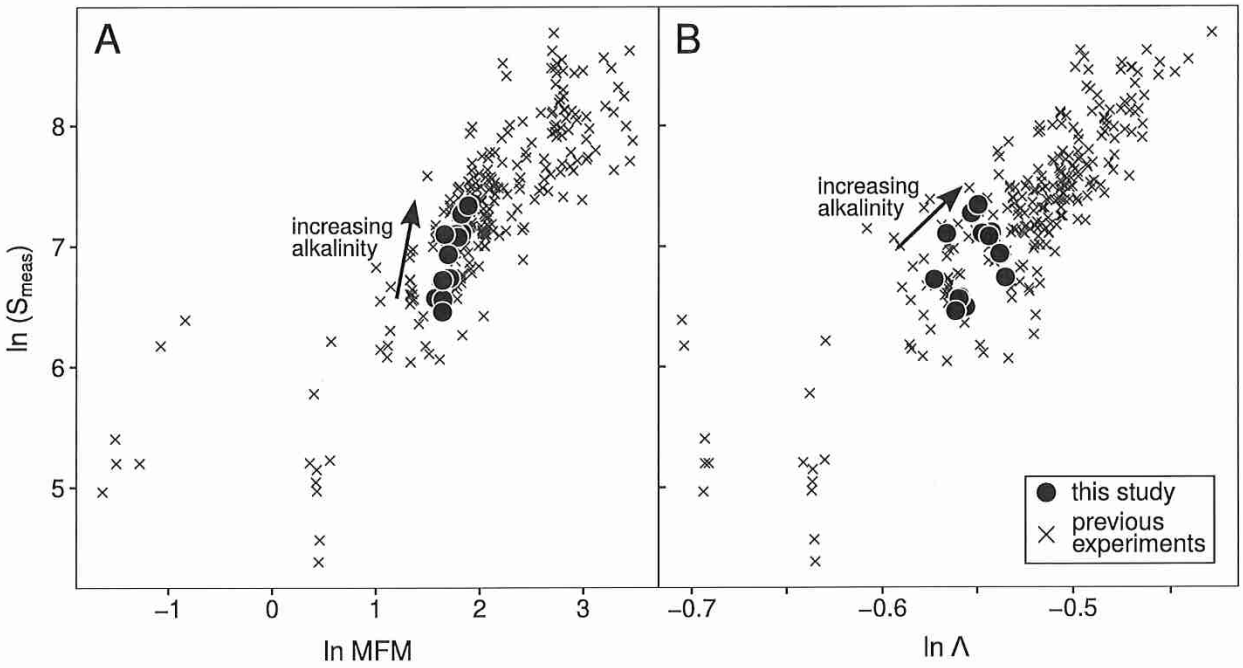

This is a preprint, the final version is subject to change, of the American Mineralogist (MSA)
Cite as Authors (Year) Title. American Mineralogist, in press.
DOI: https://doi.org/10.2138/am-2018-6404

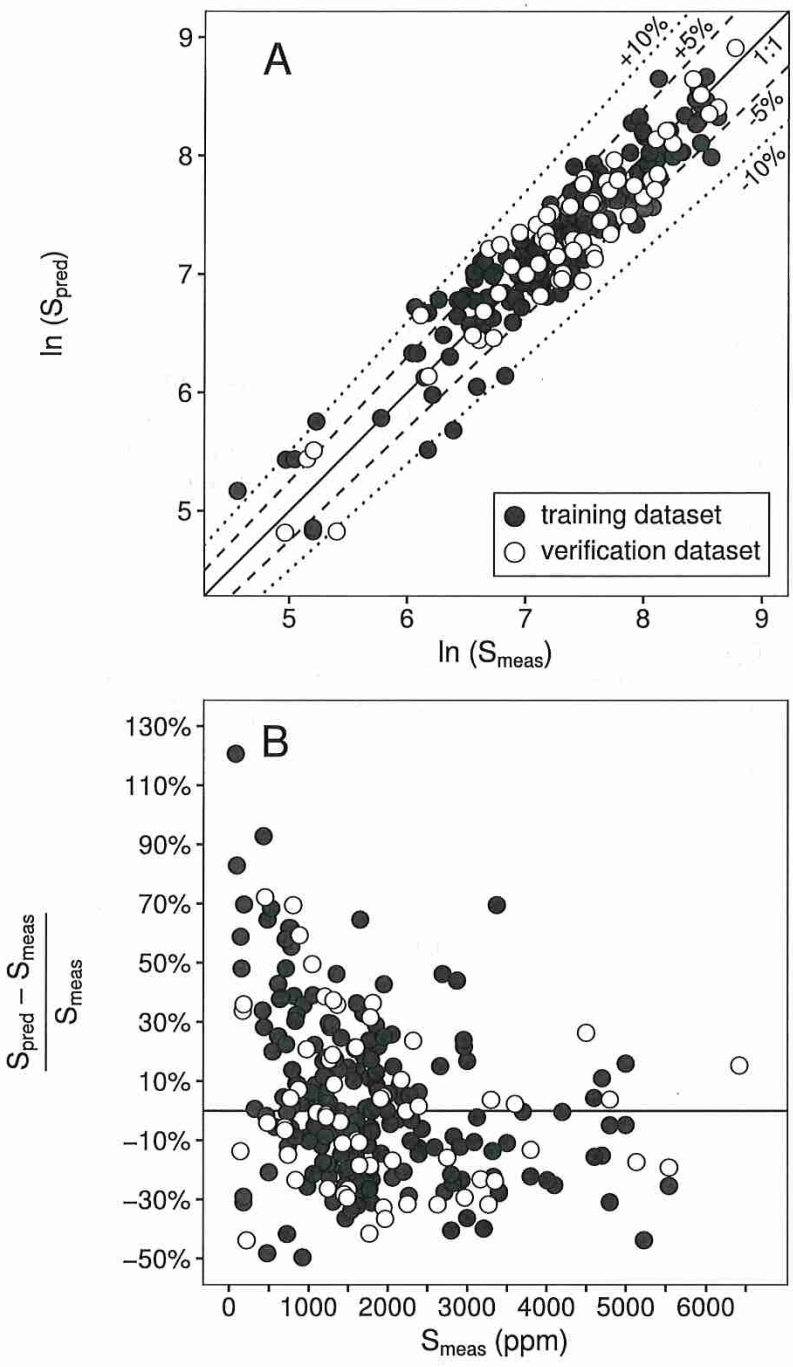

This is a preprint, the final version is subject to change, of the American Mineralogist (MSA)
Cite as Authors (Year) Title. American Mineralogist, in press.
DOI: https://doi.org/10.2138/am-2018-6404

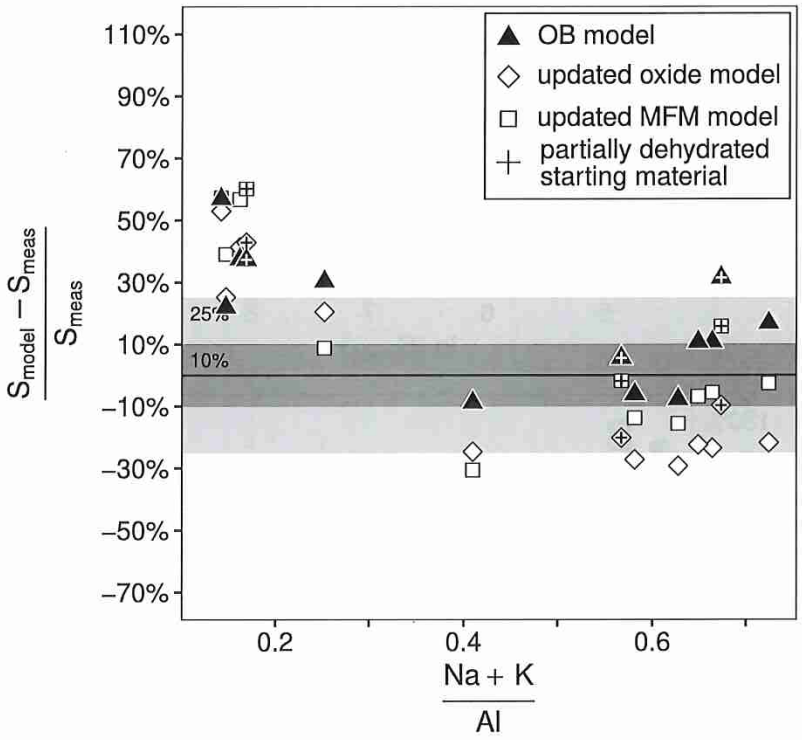

DOI: https://doi.org/10.2138/am-2018-6404

Table 1. Starting material compositions

	RD0K	RD1K*	RD3K**	RD4K	RD6K	GUM80-94[a]	JAL-07-35[b]
SiO_2	51.23	51.24	51.25	51.37	51.27	53.37	50.1
TiO_2	0.51	0.61	0.77	1.03	1.02	0.43	1.7
Al_2O_3	18.73	18.23	17.47	16.22	16.20	17.9	12.4
FeO^{tot}	7.38	7.06	6.58	6.84	5.78	7.58	6.8
MgO	4.60	4.30	3.84	3.59	3.08	8.21	9.6
CaO	11.27	10.87	10.25	9.25	9.23	10.09	7.2
Na_2O	1.54	1.74	2.05	3.08	2.56	1.97	2.2
K_2O	0.00	1.23	3.08	4.11	6.15	0.15	6.3
H_2O	3.50	3.50	3.49	3.50	3.49	1.37	0.7
S	1.02	1.01	1.00	1.00	0.99	-	-
P2O5	-	-	-	-	-	0.06	1.6
MnO	-	-	-	-	-	0.13	0.1
total	99.79	99.79	99.79	100.00	99.79	101.26	98.74

* RD1K is a 4:1 mixture (by weight) of RD0K and RD6K

** RD3K is a 1:1 mixture (by weight) of RD0K and RD6K

[a] example of natural basaltic andesite, Guam (Regan *et al.*, 2008)

[b] example of natural shoshonite (Gomez-Tuena *et al.*, 2011)

Table 2: Experimental conditions and resulting phases

Run #	duration (h)	SM-new	phases present	log f_{O2}	ΔFMQ
P466	1	RD-6K	liq, sulf	-9.35	-2.55
P468	1	RD-0K	liq, sulf, px	-9.35	-2.55
P470	4	RD-0K	liq, sulf	-9.35	-2.55
P471	4	RD-0K*	liq, sulf, px	-9.35	-2.55
P472	4	RD-6K*	liq, sulf	-9.35	-2.55
P474	4	RD-6K	liq, sulf	-9.35	-2.55
P478	4	RD-4K*	liq, sulf	-9.35	-2.55
P476	4	RD-4K	liq, sulf	-9.35	-2.55
P479	4	RD-3K	liq, sulf, Pt wire	-9.2	-2.4
P480	4	RD-1K	liq, sulf, Pt wire	-9.5	-2.7

Abbreviations: liq = liquid; sulf = sulfide droplet; px = pyroxene.
*starting material partially dehydrated prior to use

Table3

Tabl

Run	lab	SM	t (h)	SiO_2	TiO_2	Al_2O_3	FeO^{tot}
P466	UBC	RD6K	1	52.38 (0.95)	1.12 (0.03)	15.96 (0.60)	4.54 (0.15)
P466	UA	RD6K	1	53.37 (0.58)	1.09 (0.04)	16.42 (0.64)	4.43 (0.11)
P468	UBC	RD0K	1	54.50 (1.61)	0.61 (0.06)	17.60 (0.38)	6.30 (0.46)
P468	UA	RD0K	1	55.27 (1.52)	0.60 (0.05)	18.32 (0.26)	6.05 (0.19)
P470	UA	RD0K	4	52.82 (0.59)	0.58 (0.04)	19.48 (0.22)	5.47 (0.10)
P471	UA	RD0K*	4	55.98 (1.26)	0.59 (0.03)	17.28 (0.54)	5.71 (0.81)
P472	UA	RD6K*	4	53.49 (0.48)	1.12 (0.03)	16.65 (0.14)	4.44 (0.08)
P474	UA	RD6K	4	52.98 (0.70)	1.15 (0.03)	16.41 (0.06)	4.11 (0.04)
P476	UBC	RD4K	4	53.05 (0.75)	1.12 (0.08)	15.55 (0.33)	5.12 (0.40)
P476	UA	RD4K	4	54.08 (0.43)	1.11 (0.04)	16.30 (0.07)	4.95 (0.15)
P478	UA	RD4K*	4	53.42 (0.19)	1.11 (0.05)	17.32 (0.11)	5.08 (0.03)
P479	UBC	RD3K	4	54.70 (0.83)	0.90 (0.08)	18.02 (0.25)	1.85 (0.33)
P480	UBC	RD1K	4	54.66 (0.56)	0.73 (0.04)	18.69 (0.23)	2.27 (0.26)
VG-2 analyses (n = 18)				49.68 (0.52)	1.86 (0.12)	13.35 (0.43)	11.67 (0.55)
VG-2 reference values[c]				50.81	1.85	14.06	11.82

values in parentheses are 2σ error
*starting material partially dehydrated prior to use
** measured by Raman
[a] calculated as per Kress and Carmichael (1991)
[b] calculated as per Mills (1993) and Duffy (1996); see text and Supplementary table
[c] Smithsonian microbeam standard NMNH 111240-52 recommended values; S con

This is a preprint, the final version is subject to change, of the American Mineralogist (MSA)
Cite as Authors (Year) Title. American Mineralogist, in press.
DOI: https://doi.org/10.2138/am-2018-6404

Table3

e 3: Composition of glasses determined by EPMA (wt.% except S, ppm)

MgO	CaO	Na_2O	K_2O	S (ppm)	Sum	difference from 100%
3.08 (0.06)	9.54 (0.20)	2.72 (0.12)	6.53 (0.15)	1225 (66)	96.02 (1.17)	3.98
3.14 (0.08)	9.51 (0.12)	2.52 (0.07)	6.24 (0.07)	1214 (73)	96.85 (0.89)	3.15
4.67 (0.27)	11.6 (0.38)	1.68 (0.16)	0.08 (0.03)	660 (93)	97.11 (1.79)	2.89
4.75 (0.34)	11.46 (0.42)	1.60 (0.18)	0.07 (0.02)	714 (78)	98.19 (1.65)	1.81
4.95 (0.07)	12.05 (0.09)	1.64 (0.02)	0.07 (0.01)	705 (19)	97.13 (0.65)	2.87
5.03 (0.22)	11.5 (0.16)	1.72 (0.09)	0.08 (0.01)	637 (47)	97.96 (1.62)	2.04
3.31 (0.02)	9.83 (0.15)	2.70 (0.03)	6.25 (0.07)	842 (109)	97.88 (0.54)	2.12
3.36 (0.03)	10.16 (0.09)	2.51 (0.03)	6.01 (0.09)	1184 (56)	96.82 (0.71)	3.18
3.75 (0.11)	9.95 (0.17)	3.07 (0.11)	4.34 (0.14)	1537 (45)	96.1 (0.96)	3.9
3.81 (0.09)	9.88 (0.16)	2.98 (0.02)	4.22 (0.09)	1434 (45)	97.48 (0.51)	2.52
3.76 (0.06)	10.00 (0.06)	3.17 (0.04)	4.26 (0.07)	1025 (44)	98.22 (0.25)	1.78
4.18 (0.21)	11.33 (0.30)	2.28 (0.11)	3.35 (0.13)	1211 (113)	96.73 (1.01)	3.27
4.70 (0.09)	12.05 (0.21)	1.95 (0.14)	1.40 (0.06)	828 (27)	96.53 (0.72)	3.47
6.9 (0.22)	10.84 (0.27)	2.59 (0.22)	0.21 (0.04)	1521 (81)	97.10 (1.94)	
6.95	11.12	2.62	0.19	1397 (172)	99.42	

› 3 for details
ıcentration is the average of all reported analyses

This is a preprint, the final version is subject to change, of the American Mineralogist (MSA)
Cite as Authors (Year) Title. American Mineralogist, in press.
DOI: https://doi.org/10.2138/am-2018-6404

Table3

H_2O**	Fe_2O_3/FeO[a]	(Na+K)/Al	Na/(Na+K)	Λ[b]
2.84 (0.38)	0.034	0.724	0.388	0.581
2.84 (0.38)	0.033	0.664	0.380	0.578
1.19 (0.16)	0.025	0.162	0.969	0.573
1.19 (0.16)	0.025	0.147	0.972	0.572
2.43 (0.32)	0.025	0.142	0.972	0.571
1.38 (0.19)	0.026	0.169	0.970	0.570
1.31 (0.17)	0.034	0.673	0.396	0.585
2.58 (0.35)	0.034	0.649	0.389	0.580
3.14 (0.42)	0.032	0.627	0.518	0.577
3.14 (0.42)	0.031	0.581	0.518	0.575
1.28 (0.17)	0.032	0.567	0.530	0.584
-	0.033	0.410	0.508	0.568
-	0.027	0.252	0.679	0.564

This is a preprint, the final version is subject to change, of the American Mineralogist (MSA)
Cite as Authors (Year) Title. American Mineralogist, in press.
DOI: https://doi.org/10.2138/am-2018-6404

Table4

Table 4: Updated and original parameters for MFM and oxide models from Fortin et al. error in parentheses.

MFM			oxide model	
Parameter	Coefficient*	Coefficient**	Parameter	Coefficient*
Intercept	10.55 (0.47)	10.430 (0.428)	Intercept	36.05 (10.67)
1/T	-5081 (578)	-4981.6 (532.7)	1/T	-6115 (471)
P/T	-366.7 (57.5)	-332.37 (54.01)	P/T	-363.3 (40.2)
ln[MFM]	0.4653 (0.0461)	0.45280 (0.03910)	X_{H2O}	-21.01 (10.70)
lnX_{FeO}	0.3276 (0.0392)	0.32270 (0.03650)	X_{SiO2}	-26.68 (10.65)
X_{H2O}	2.967 (0.578)	3.7449 (0.5663)	X_{TiO2}	-19.97 (11.03)
			X_{Al2O3}	-27.34 (9.97)
			X_{FeOtot}	-18.10 (10.73)
			X_{MgO}	-23.71 (10.60)
			X_{CaO}	-21.08 (10.85)
			X_{Na2O}	-23.51 (11.50)
			X_{K2O}	-26.69 (10.34)
$R^2_{training}$	0.791	0.807	$R^2_{training}$	0.904
$X^2_{training}$	3.29	3.71	$X^2_{training}$	1.49
$R^2_{verification}$	0.855		$R^2_{verification}$	0.929
$X^2_{verification}$	0.879		$X^2_{verification}$	0.432

* this study
** Fortin *et al.* (2015)
coefficients and standard error provided to greater-than-significant digits to avoid round

Table4

(2015); standard

Coefficient**
34.784 (7.089)
-5772.3 (407.85)
-346.54 (37.39)
-20.393 (7.109)
-25.499 (7.068)
-18.344 (7.331)
-27.381 (6.683)
-17.275 (7.159)
-22.398 (7.003)
-20.378 (7.242)
-18.954 (7.445)
-32.194 (7.556)
0.918
1.46

l-off errors.

This is a preprint, the final version is subject to change, of the American Mineralogist (MSA)
Cite as Authors (Year) Title. American Mineralogist, in press.
DOI: https://doi.org/10.2138/am-2018-6404

Table 5: OB model parameters

Parameter (label)*	Coefficient	Std. Error
Intercept (a)	16.44	0.41
1/T (b)	-6081	446
P/T (c)	-379.8	45.8
ln[Λ] (d)	10.61	0.67
X_{FeO} (e)	3.533	0.563
X_{H2O} (f)	6.601	0.472

$R^2_{training} = 0.865$

$X^2_{training} = 2.13$

$R^2_{verification} = 0.903$

$X^2_{verification} = 0.615$

* labels refer to equation [8] in text